A novel sea surface pCO$_2$-product for the global coastal ocean resolving trends over the 1982-2020 period

Alizée Roobaert[1], Pierre Regnier[1], Peter Landschützer[2] and Goulven G. Laruelle[1]

[1]Department of Geosciences, Environment & Society-BGEOSYS, Université Libre de Bruxelles, Brussels, CP160/02, Belgium

[2]Flanders Marine Institute (VLIZ), Ostend, Belgium

Correspondence to: Alizée Roobaert (alizee.roobaert@ulb.be)

Abstract

In recent years, advancements in machine learning based interpolation methods have enabled the production of high-resolution maps of sea surface partial pressure of CO$_2$ (pCO$_2$) derived from observations extracted from databases such as the Surface Ocean CO$_2$ Atlas (SOCAT). These pCO$_2$-products now allow quantifying the oceanic air-sea CO$_2$ exchange based on observations. However, most of them do not yet explicitly include the coastal ocean. Instead, they simply extend the open ocean values onto the nearshore shallow waters, or their spatial resolution is simply so coarse that they do not accurately capture the highly heterogeneous spatiotemporal pCO$_2$ dynamics of coastal zones. Until today, only one global pCO$_2$-product was specifically designed for the coastal ocean (Laruelle et al., 2017). This product however has shortcomings because it only provides a climatology covering a relatively short period (1998-2015), thus hindering its application to the evaluation of the interannual variability and the long-term trends of the coastal air-sea CO$_2$ exchange, a temporal evolution that is still poorly understood and highly debated. Here we aim at closing this knowledge gap and update the coastal product of Laruelle et al. (2017) to investigate the longest global monthly time series available for the coastal ocean from 1982 to 2020. The method remains based on a 2-step Self Organizing Maps and Feed Forward Network method adapted for coastal regions, but we include additional environmental predictors and use a larger pool of training and validation data with ~ 18 million direct observations extracted from the latest release of the SOCAT database. Our study reveals that the coastal ocean has been acting as an atmospheric CO$_2$ sink of -0.4 Pg C yr^{-1} (-0.2 Pg C yr^{-1} with a narrower coastal domain) on average since 1982, and the intensity of this sink has increased at a rate of 0.1 Pg C yr^{-1} decade^{-1} (0.03 Pg C yr^{-1} decade^{-1} with a narrower coastal domain) over time. Our results also show that the temporal trend in the air-sea pCO$_2$ gradient plays a significant role in the decadal evolution of the coastal CO$_2$ sink, along with wind speed and sea-ice coverage changes that can also play an important role in

30   some regions, particularly at high latitudes. This new reconstructed coastal pCO$_2$-product (Roobaert et al., 2023, https://www.ncei.noaa.gov/archive/accession/0279118) allows establishing regional carbon budgets requiring high-resolution coastal flux estimates and provides new constraints for closing the global carbon cycle.

Short summary

35   Advancements in understanding the coastal air-sea CO$_2$ exchange (FCO$_2$) have been made, but long-term temporal trends remain unclear. Our research, based on observations and a machine learning approach, reconstructs the longest global time series of coastal FCO$_2$ (1982 to 2020). Results show the coastal ocean acts as a CO$_2$ sink, with increasing intensity over time. This new coastal FCO$_2$ product allows establishing regional carbon budgets and provides new constraints for closing the global carbon cycle.

40   **1 Introduction**

The exchange of carbon dioxide (CO$_2$) between the atmosphere and the ocean depends on the gradient between the partial pressure of CO$_2$ (pCO$_2$) at the surface of the ocean and that of the overlying air. Over the past decade, the number of high-quality measurements of sea surface pCO$_2$ collected by research field programs and ships of opportunities have considerably increased. Moreover, large-scale community efforts have led to the compilation of tens of millions of sea surface pCO$_2$

45   measurements into uniform quality-controlled databases such as SOCAT (for Surface Ocean CO$_2$ Atlas, Bakker et al., 2014), allowing for the quantification of the global oceanic CO$_2$ sink. However, in spite of this tremendous increase in data coverage, once gridded monthly at a typical spatial resolution of 1° for the open ocean and 0.25° for the coastal ocean, pCO$_2$ measurements remain largely discontinuous in time and space. The remaining regions and periods of time devoid of data thus prevent one from fully quantifying the air-sea CO$_2$ exchange and its full spatiotemporal variability based on measurements

50   alone.

Therefore, in parallel to the on-going measurement synthesis efforts, another research branch aiming at developing robust interpolation techniques to circumvent the spatial and temporal gaps in the data products has emerged. These techniques allow creating maps of pCO$_2$ that are continuous in space and time, typically at the monthly resolution (e.g., Chau et al., 2022; Gloege

55   et al., 2022; Gregor & Gruber, 2021; Landschützer et al., 2014; Rödenbeck et al., 2014, 2015). The resulting observation-based continuous products (called hereafter 'pCO$_2$-products') however differ in their spatial resolutions (e.g., from 0.25°x 0.25° in Chau et al. (2023) over 1° x 1° in Landschützer et al., 2014 to 4° x 5° in Majkut et al., 2014), their temporal coverage and their method of interpolation. Several studies have relied on direct interpolations of available pCO$_2$ measurements (e.g., Jones et al., 2015; Rödenbeck et al., 2014; Shutler et al., 2016) while others have first established linear (e.g., Iida et al., 2015; Park et

60   al., 2010; Schuster et al., 2013) or nonlinear (e.g., Landschützer et al., 2014; Nakaoka et al., 2013; Zeng et al., 2014) predictive regression equations between a set of environment parameters (available everywhere and at everytime within the domain of

interest) and observed pCO$_2$ to perform the spatiotemporal extrapolation. These complementary pCO$_2$-products provide a better quantification of the spatial and temporal variability of the global oceanic CO$_2$ sink and its associated uncertainty on different time scales, going from seasonal fluctuations to decadal trends through interannual variability, while providing much

65   improved observation-based benchmarks against which outputs from global model results can be evaluated (e.g., Hauck et al., 2020).

While significant efforts have been invested by the community to develop pCO$_2$-products for the global ocean, leading to a growing number of assessments of the CO$_2$ sink, most of these pCO$_2$-products ignore the coastal ocean (e.g., Landschützer et

70   al., 2014) or resolve it by simply combining the coast with the open ocean (Chau et al., 2023). Indeed, the spatiotemporal investigations are performed for the entire ocean using the full set of observed pCO$_2$ data (coast and open ocean) in such a way that the specific conditions characteristic of coastal settings are not accurately accounted for in these products (e.g., Chau et al., 2022; Rödenbeck et al., 2013). In response to this shortcoming, other continuous pCO$_2$-products have been developed at the regional scale for several well monitored coastal seas (e.g., Bai et al., 2015; Hales et al., 2012; Jamet et al., 2007; Ono et

75   al., 2004; Sarma et al., 2006) such as the California Current system (Sharp et al., 2022), European shelves (Becker et al., 2021) or the West Florida shelf (Chen et al., 2016). At the global scale, a significant step forward was made by Laruelle et al. in 2017 when the first global coastal pCO$_2$-product at high spatial resolution (0.25°) was released for the entire coastal domain. This product, which is still, to date, the only one available specifically developed for the global coastal ocean, is based on gridded coastal pCO$_2$ observations and nonlinear predictive regression equations between a set of environmental variables (drivers)

80   and observed pCO$_2$ to perform the spatiotemporal extrapolation (the Self Organizing Map and Feed Forward Network coastal pCO$_2$-product, ULB-SOM-FFN-coastalv1, Laruelle et al., 2017). This global coastal pCO$_2$-product provided a climatological mean (period 1998-2015) which allowed unprecedented investigation of the spatial distribution of the CO$_2$ sources and sinks in the global coastal ocean, especially for regions lacking data or regional assessments. It also allowed resolving the seasonal variability of the air-sea CO$_2$ exchange in the coastal domain (Roobaert et al., 2019). Moreover, it was recently merged with

85   an open ocean product to obtain a global reconstruction of the ocean CO$_2$ sink (Landschützer et al., 2020) and has been subsequently used to reduce the spread in global reconstructions (Fay et al., 2021). However, the ULB-SOM-FFN-coastalv1 pCO$_2$-product remains limited in its applications because it only provides a climatology covering a relatively short period (1998-2015) and is thus not suitable to evaluate the interannual variability or the long-term trends of the coastal air-sea CO$_2$ exchange. Such questions currently are at the forefront of the coastal research community's preoccupations (Bauer et al., 2013;

90   Lacroix et al., 2021a; Laruelle et al., 2018; Regnier et al., 2013; Resplandy et al., in rev.; Wang et al., 2017) but, because of the lack of adequate product, our confidence in the extent to which humans have perturbed the coastal air-sea CO$_2$ exchange since pre-industrial times remains low (Regnier et al., 2022). Moreover, the limitations of the ULB-SOM-FFN-coastalv1 do not yet allow producing robust trends in coastal pCO$_2$ fields against which global model outputs can be evaluated (e.g., Resplandy et al., in rev.).

95

To address these limitations, this study expands and improves upon the version of the global coastal pCO_2-product of Laruelle et al. (2017) by extending its temporal coverage to four decades (1982-2020) and updating the methodology to resolve longer-terms changes in pCO_2, as described in the following section. The evaluation of this new product (ULB-SOM-FFN-coastalv2, Roobaert et al., 2023, https://www.ncei.noaa.gov/archive/accession/0279118) is done both spatially and for each decade

100   individually, which represents an improvement compared to Laruelle et al. (2017) where the ULB-SOM-FFN-coastalv1 evaluation was limited to spatial and climatological seasonal cycles only. Using ULB-SOM-FFN-coastalv2 that relies on ~ 18 million coastal direct observations from the SOCATv2022 database, we recalculate the coastal air-sea CO_2 exchange (FCO_2) for the 1982-2020 period and briefly describe the temporal evolution of the global coastal CO_2 sink over this timeframe. In the future, these updated pCO_2 and FCO_2 products can be used as benchmark for global oceanic models resolving trends in the

105   coastal CO_2 dynamics, fulfilling a key knowledge gap identified in the latest Regional Carbon Cycle Assessment and Processes coastal synthesis (RECCAP2, Resplandy et al., in rev.).

2. Methods

This section first describes the 2-step interpolation method used to generate the new version of the coastal pCO_2-product (Sect. 2.1) and the different datasets involved in this two steps procedure (Sect. 2.2). We then describe how the coastal air-sea CO_2

110   exchange is calculated (Sect. 2.3) and finally explain the approach used to quantify the uncertainties associated with our new pCO_2 and FCO_2 products (Sect. 2.4).

2.1 Self Organizing Maps and Feed Forward Network

We build upon the method described in Laruelle et al. (2017) to construct an updated observation-based continuous monthly pCO_2-product for the coastal ocean (ULB-SOM-FFN-coastalv2) at a 0.25° spatial resolution over the 1982 to 2020 period.

115   The method is based on the application of two artificial neural networks (the Self Organizing Map, SOM and the Feed Forward Network, FFN). The SOM first clusters the global coastal ocean into provinces characterized by similar environmental properties. In each province, the FFN then establishes nonlinear relationships between the observed pCO_2 and a set of environmental drivers of the coastal pCO_2 dynamics (which may be different from those used by the SOM). These relationships are then used to perform the spatiotemporal extrapolation of pCO_2 in each region defined by the SOM. This method was

120   originally developed for the open ocean and is extensively described in Landschützer et al. (2013, 2014). It was later adapted for the global coastal ocean by Laruelle et al. (2017). We thus provide only a brief description of the methodology and focus here on the modifications introduced in this study.

In a first step, the global coastal ocean is divided into 10 biogeochemical provinces using the SOM clustering algorithm. Each

125   resulting province is characterized by similar spatiotemporal patterns of a set of environmental variables, or drivers. In this study, we use the same drivers as in Laruelle et al. (2017), which consist of the wind speed calculated at 10 meters above the sea surface (U_{10}), the Sea Surface Temperature (SST), the Sea Surface Salinity (SSS), the bathymetry, and the rate of change

of the sea ice coverage (see Sect. 2.2 for a description of the datasets). The SOM uses a neural network to detect similarities within multivariate datasets and uses an iterative procedure to distribute them into a predefined number of clusters. For each

130   environmental driver, continuous monthly maps at the spatial resolution of 0.25° are used as inputs for the neural network and each 0.25° cell is allocated to one of the 10 provinces (or neurons). This procedure aims at minimizing the Euclidean distance between all points within each neuron of the network (see Landschützer et al., 2013 for more details). The spatial extension of these provinces varies from one month to the other because of the seasonal variations of the environmental drivers in such a way that a fixed grid cell in space may be assigned to several provinces over the course of a year. The choice of 10 provinces

135   in the SOM stems from a sensitivity analysis that minimizes the average deviation between the observed pCO_2 and those simulated by the FFN algorithm (see second step below) while ensuring the presence of a minimum number of grid cells (>100) that can be used for the validation in each province (Laruelle et al., 2017). While their spatial extent varies seasonally, each province remains associated with specific regions over the course of the entire 1982-2020 period and the province occurring most often in each grid cell is shown in Fig. 1. Broadly, these provinces represent: Province 1 (P1) the Antarctic

140   shelf, P2-P3 two subpolar/temperate coastal provinces of the South Hemisphere, P4 and P6 the large tropical coastal provinces, P5 a temperate province of the Northern Hemisphere which includes the Mediterranean Sea and the Norwegian Sea. P7, P8 and P10 represent high latitudes of the Northern Hemisphere provinces that are seasonally partly covered by sea-ice (with the Baltic Sea and the Hudson Bay in P8) while P9 represent a permanent and cold polar province.

145   In a second step, within each biogeochemical province identified in step 1 (SOM), a FFN algorithm establishes nonlinear relationships between the observed sea surface pCO_2 and independent variables, or drivers, that are known to control its spatial and temporal variability. For each province, the FFN algorithm calculates relationships between a target variable (here pCO_2 using pCO_2 observations from the SOCAT_a dataset - see below) and inputs (environmental drivers - see below and Table 1) by adjusting weighting factors of a sigmoid activation function (one sigmoid function per neuron in the hidden layer) following

150   an iterative procedure, i.e., a Levenberg-Marquardt backpropagation algorithm. At the first iteration, the weights of neurons are randomly assigned and the estimated pCO_2 is compared with the actual pCO_2 observations. Based on the resulting mismatch, the network weights are iteratively updated in a way that the error function - in our case the mean squared error between network output and actual observations - gets minimized. For each iteration, the FFN algorithm uses a fraction of the pCO_2 observations for the actual training of the network (i.e., the adjustment of the neuron weights), while another randomly

155   selected fraction of the dataset is used to independently evaluate the performance of the algorithm. The final coefficients are obtained when the pCO_2 simulated from the validation data does not significantly improve relative to the observations, to prevent overfitting. The final neuron weights and thus the resulting input-output relationships are used to calculate pCO_2 in each cell and for each month during the 1982-2020 period.

160

The predictors used for the FFN are U_{10}, SST, SSS, the atmospheric pCO_2, the rate of change in sea ice coverage (except in regions not covered by sea ice, i.e., in P2, P3, P4 and P6), the bathymetry and the chlorophyll-a concentration (Chl-a). The Chl-a is expressed as $\log_{10}$(Chl-a) to minimize the influence of its skewed distribution (Wrobel-Niedzwiecka et al., 2022) . In P1, P8 and P9, we do not use Chl-a as a driver because of the poor data coverage resulting from recurring cloud and/or sea-ice coverage in those provinces (see Sect. 2.2). This incomplete data coverage for Chl-a is incidentally the reason why this predictor is not used at the SOM stage because it requires complete global datasets. Atmospheric pCO_2, which was not included in the ULB-SOM-FFN-coastalv1, is also used as a driver of multi-decadal changes induced by the increasing atmospheric pCO_2 concentration. Finally, we smooth spatially the monthly-resolved coastal pCO_2 field generated by the FFN using a moving 3 by 3 pixel window to remove abrupt pCO_2 transitions sometimes occurring at the boundaries between provinces. This smoothing procedure is described by Landschützer et al. (2014) and was also used in the ULB-SOM-FFN-coastalv1.

The surface pCO_2 data used by the FFN are extracted from the SOCATv2022 database (Bakker et al., 2022) that originally contains ~ 40 million pCO_2 measurements for the entire global ocean (open and coastal seas combined). We follow the recommendation of the SOCAT community and use their accuracy criteria to only retain the data with the highest accuracy. To do so, we first select sea surface measurements expressed in fugacity of CO_2 (fCO_2) with a quality flag ranging from A to D (which corresponds to an estimated accuracy better than 5 µatm) and a World Ocean Circulation Experiment (WOCE) flag of 2 (good dataset following SOCAT) for the 1982-2020 period. Following Laruelle et al. (2017), we also remove fCO_2 values < 30 µatm and > 1000 µatm that are likely derived from estuarine or fresh water systems that are not included in our coastal domain. We then randomly divide this dataset rich of ~ 32 million fCO_2 measurements into a group of data used for the FFN algorithm ('a', 80 % of the original dataset) and a group of data that we use to validate our reconstructed pCO_2 ('b', 20 % of the original dataset). The two sets of data (SOCAT_a and SOCAT_b) are then gridded for each month at 0.25° using the average of all fCO_2 values in each cell. Values are then converted from fCO_2 to pCO_2 using the equation of Takahashi et al. (2012, page 6) and a coastal mask is applied on both gridded pCO_2 products. In this study, the coastal domain (total surface area of 76 million km², Laruelle et al., 2017) excludes the Black Sea, estuaries as well as inland water bodies and its outer limit is defined as whichever point is furthest from the shoreline between the 1000 m isobath and a fixed 300 km distance (roughly the outer edge of territorial waters), following the coarse SOCAT definition of the coastal oceanic domain. At the end of this entire procedure, a total of ~ 14 million and ~ 4 million coastal data have been allocated to SOCAT_a and SOCAT_b, respectively.

2.2 Environmental variables

The observational SST and SSS fields used as inputs for the SOM-FFN algorithm are calculated as the monthly means of the daily NOAA OI SST V2 (Reynolds et al., 2007) and of the daily Hadley center EN4 SSS (Good et al., 2013), respectively (Table 1). For U_{10}, we use the monthly mean of the 0.25° resolution product of the global atmospheric reanalysis ERA-interim wind product (Dee et al., 2011), which has a native temporal resolution of 6 hours. The monthly mean of the daily 0.25° dataset

of Reynolds et al. (2007) is used for the sea-ice coverage. The rate of change in the sea-ice coverage for a given month x is then calculated as the difference between the sea-ice coverages of months x+1 and x-1. The atmospheric pCO_2 is calculated from the dry air mixing ratio of CO_2 (xCO_2) provided by the NOAA Marine Boundary Layer reference product (https://www.esrl.noaa.gov/gmd/ccgg/mbl/) assuming 100 % humidity at the air-sea interface (following calculation specified in Dickson et al., 2007) and using the NCEP reanalysis total pressure at sea level (Kalnay et al., 1996). It should be noted that, due to the proximity to the continent of the coastal ocean, the latter might be more exposed to anthropogenic sources of CO_2 and thus higher atmospheric pCO_2 compared with the global oceanic average. The use of spatially resolved dry air mixing ratio of CO_2 datasets such as the one from the NASA's Orbiting Carbon Observatory 2 Goddard Earth Observing System (OCO-2 GEOS, Eldering et al., 2017) instead of the product used in this study might be more appropriate to include this effect. However, OCO-2 GEOS only covers the 2015-2022 period, which is too short for the purpose of our study. It is also expected that the choice of the atmospheric pCO_2 does not considerably influence our FCO_2 calculations as the air-sea pCO_2 difference is mainly controlled by the oceanic pCO_2 (see Sect. 2.4). We use the bathymetry from the 2 min global ETOPO2 database (US Department of Commerce, 2006) and the Chl-a field derived from the monthly 4 km merged globcolour product from the U.U Copernicus Marine Service information (https://doi.org/10.48670/moi-00281), which is the product with the longest Chl-a temporal coverage (1998-2020 period). However, because of recurrent cloud coverage everywhere and sea-ice coverage at high latitudes, the monthly averaged Chl-a field at a 0.25° resolution is discontinuous with grid cells devoid of data. We fill these cells (9 % excluding high latitude coastal regions) using a cascade of interpolation methods, which order depends on data availability in time and space in the surrounding cells : for an empty cell of the month x, the interpolation is performed by computing (1) the mean of the next neighboring cells of the month x, (2) the mean value of the month x+1 and month x-1 of the same cell, (3) the monthly mean value x of the cell for the entire 1998-2020 period, (4) the annual mean value of the cell for the entire 1998-2020 period. At high latitudes, where none of these options are feasible because of large bands without any data, we assign the modal value of Chl-a as default value in order to ensure the continuity of the maps that is required for the FFN algorithm. From this continuous gridded Chl-a product over the recorded period, we then calculate for each cell a monthly seasonal climatology and attribute the climatological values to the unrecorded period (1982-1997). This means that, in our calculations, Chl-a does not contribute to long-term changes in pCO_2 before 1997. All observational fields are converted from their original spatiotemporal resolution to monthly 0.25° gridded resolution for the 1982-2020 period (except for the bathymetry which is constant over time) to match the observational pCO_2 product (SOCAT_a) resolution (Table 1).

2.3 Air-sea CO_2 exchange

The pCO_2 field generated by the SOM-FFN algorithm (ULB-SOM-FFN-coastalv2) is used to calculate the air-sea CO_2 exchange for each grid cell at the monthly time scale over the 1982-2020 period following Eq. (1):

$$FCO_2 = k \, K_0 \, \Delta pCO_2 \, (1 - ice) \tag{1}$$

where FCO_2 (mol C m^{-2} yr^{-1}) represents the coastal air-sea CO_2 exchange, ΔpCO_2 (atm) is the gradient between the oceanic pCO_2 and the atmospheric pCO_2 and K_0 (mol m^{-3} atm^{-1}) is the CO_2 solubility in seawater which is a function of SST and SSS following the equation of Weiss (1974). k (m yr^{-1}) represents the gas exchange transfer velocity which is a function of the second moment of the wind speed at 10 meters above sea level and is calculated using the equation of Ho et al. (2011) and using the Schmidt number based on the equation of Wanninkhof (2014). The sea-ice coverage for each grid cell is represented by the term ice and ranges from 0 (no ice cover) to 1 (100 % ice cover). By convention a positive FCO_2 value corresponds to a source of CO_2 for the atmosphere. We use the same U_{10}, SST, SSS, sea-ice coverage and atmospheric pCO_2 datasets (see Sect. 2.2) to calculate FCO_2 and perform the FFN pCO_2-reconstruction. Our reconstructed coastal FCO_2 is also compared with coastal FCO_2 estimates derived from a synthesis of 214 regional FCO_2 estimations (Dai et al., 2022) and from the FCO_2-product derived from the original ULB-SOM-FFN-coastalv1 pCO_2-product (Roobaert et al., 2019).

2.4 Uncertainties of the reconstructed coastal data-products

The uncertainties associated with our reconstructed pCO_2 and FCO_2 coastal products are estimated using the method proposed by Landschützer et al. (2014, 2018) and used by subsequent authors (e.g., Roobaert et al., 2019; Sharp et al., 2022). The FCO_2 uncertainty results from four sources of uncertainties, which are considered independent and thus summed quadratically:

$$\sigma_{FCO_2} = \sqrt{\sigma_{\Delta pCO_2}^2 + \sigma_k^2 + \sigma_{wind}^2 + \sigma_{ice}^2} \tag{2}$$

Where σ_{FCO_2} represents the total FCO_2 uncertainty (Petagrams of Carbon per year, Pg C yr^{-1}), $\sigma_{\Delta pCO_2}$ is the uncertainty of the air-sea pCO_2 gradient, σ_k is the uncertainty associated with the choice of the k-formulation in Eq. (1) and σ_{wind} is the uncertainty associated with the choice of the wind speed product (see Roobaert et al., 2018). We also include the effect of the choice of sea-ice product on the FCO_2 uncertainty (σ_{ice}) which was not included in the original calculations of Landschützer et al. (2014, 2018) but has been identified as a potential source of uncertainty in global coastal reconstructions (e.g., Resplandy et al., in rev.). All of these four sources of uncertainty are expressed in Pg C yr^{-1}. σ_{wind} is calculated following the strategy described in Roobaert et al. (2018) which consists of using the standard deviation of global FCO_2 fields calculated with 3 different wind products: the ERA-interim (Dee et al., 2011), the Cross-Calibrated Multi-Platform Ocean Wind Vector 3.0 (Atlas et al., 2011) and the NCEP/NCAR reanalysis 1 (Kalnay et al., 1996). σ_k is estimated as the standard deviation of global FCO_2 fields calculated with four different global-scale k-parametrizations with the same wind speed (ERA-interim). We use the formulations of Ho et al. (2011), Sweeney et al. (2007), Takahashi et al. (2009), and Wanninkhof (2014); all suited for global scale applications (see e.g., Roobaert et al., 2018). σ_{ice} is calculated as the standard deviation of global FCO_2 fields calculated with 2 different sea-ice products: The NOAA dataset of Reynolds et al. (2007) and the sea-ice dataset of Rayner et

al. (2003). $\sigma_{\Delta pCO_2}$ mainly results from the oceanic pCO$_2$ uncertainty since the atmospheric pCO$_2$ uncertainty is significantly lower (Landschützer et al., 2018). For instance, Roobaert et al. (2019) quantified that uncertainties in atmospheric pCO$_2$ only contribute to 6 % in the overall FCO$_2$ uncertainty.

260

Following Landschützer et al. (2014), the uncertainty over the oceanic pCO$_2$ can be obtained from the quadratic sum of 3 sources of uncertainties:

$$\theta_{pCO_2} = \sqrt{\left(\frac{\theta_{obs}}{\sqrt{N}}\right)^2 + \left(\frac{\theta_{grid}}{\sqrt{N}}\right)^2 + \left(\frac{\theta_{map}}{\sqrt{N_{eff}}}\right)^2} \tag{3}$$

265

Where θ_{pCO_2} represents the total uncertainty of the oceanic pCO$_2$ (µatm), θ_{obs} is the experimental uncertainty associated with the sampling on the field of the observations from the SOCAT database (µatm), θ_{grid} is the uncertainty associated with the gridding of the observations from SOCAT into 0.25° monthly meshed maps (µatm) and θ_{map} is the uncertainty derived from the comparison between the reconstructed pCO$_2$ and the observed gridded pCO$_2$ from the SOCAT database (µatm). Following

270 Sharp et al. (2022), we use accuracies that are attributed to each fCO$_2$ measurement by the SOCAT community (flags A to D) to calculate θ_{obs}. Flags 'A' and 'B' represent an estimated accuracy of 2 µatm while the accuracy of flags 'C' and 'D' is 5 µatm. We first calculate the mean of all fCO$_2$ flags in each grid cell for each month. We then calculate the global average gridded flags uncertainty of all cells for the year x (or the entire period). For θ_{grid}, we first calculate in each grid cell of the month x the standard deviations of all fCO$_2$ values from the SOCAT database used for the gridding. We then calculate the

275 average of these standard deviations of all grid cells for the year x (or the entire period). θ_{map} is calculated as the root mean squared deviation between the reconstructed pCO$_2$ and the gridded pCO$_2$ observation from SOCAT. We also divide each source of uncertainty (i.e., θ_{obs}, θ_{grid} and θ_{map}) by the square root of the number of pCO$_2$ samples (N, see Landschützer et al., 2018; Roobaert et al., 2019 for details). For θ_{map}, the value of N is corrected to account for the fact that all individual errors are not spatially independent. To this end, we calculate the effective sample size (N$_{eff}$, see Landschutzer et al., 2018) by

280 randomly selecting 1000 samples (40 % of the samples if the total number of samples is < 1000) that cover our study period and calculating a lag 1 autocorrelation coefficient following equations (18) and (19) of Landschützer et al. (2018). As we only use a subset of 1000 samples, we perform Monte Carlo simulations where this procedure is repeated 10 times and our final N$_{eff}$ is calculated as the median of the 10 iterations. Finally, the total uncertainty on FCO$_2$ associated with the reconstructed pCO$_2$ ($\sigma_{\Delta pCO_2}$, Pg C yr^{-1}) is obtained by applying θ_{pCO_2} (µatm) in Eq. (1). All these procedures are performed globally for each

285 year and for the entire period of our study.

3 Results and discussion

3.1 pCO₂-product evaluation

Globally, our reconstructed coastal pCO₂-product compares well with the observed pCO₂ used to train the FFN algorithm (SOCAT_a) and reproduces all the well-known global spatial pCO₂ patterns with generally low pCO₂ (< 360 µatm) at
290   temperate as well as high latitudes and high pCO₂ (> 360 µatm) at low latitudes (contrast Fig. 2a with Fig. 2b). The spatial distribution of the temporal mean residuals (i.e., difference between the coastal pCO₂-product and SOCAT_a in each grid cell for every month where observations are available) reveals that, in some regions, underestimations (negative mean residual, blue colors in Fig. 2c) or overestimations (red colors) of the pCO₂ can be generated by the coastal pCO₂-product. However, most of the calculated residuals fall within the -20 to 20 µatm range, accounting for 68 % of the grid cells, while 44 % of the
295   grid cells have absolute residuals < 10 µatm (Fig. 2c and Fig. 3a).

A global mean of the residuals (bias) value of 0 µatm and a r² of 0.7 are calculated, as expected since the algorithm minimizes the Root Mean Square Error (RMSE) between measurements and target observations. The global RMSE is however, substantially larger (29 µatm) yet still comparable to those calculated, at the regional scale, in previous coastal pCO₂ studies
300   based on statistical interpolations (see e.g., Chen et al., 2016) and slightly lower than the global RMSE calculated by Laruelle et al. (2017, 32 µatm). Large differences can be observed between our product and SOCAT_a locally in regions that are known to present large spatiotemporal variabilities in pCO₂ and/or in regions lacking data to train our FFN algorithm. For instance, residuals and/or standard deviations > 20 µatm are encountered in the Baltic Sea (which is hence later treated as an independent biogeochemical province for some calculations), in upwelling regions (e.g., along the Peruvian upwelling), in coastal seas
305   under the influence of seasonal changes in sea ice coverage (e.g., along the Antarctica shelf) as well as along the very nearshore coastal domain (e.g., along the California current coast, Figs. 2c, d).

The overall consistency between our coastal pCO₂-product and SOCAT_a is diagnosed over the entire timespan of our study, as illustrated by the histograms of residuals calculated for each of the four decades of our calculation period (Fig. 3a) or when
310   the calculations are performed for each individual year (Table S1). This is an important test as a study by Gloege et al. (2022) suggests that decadal trends in pCO₂ products may be obscured by changing residual distributions over time. In spite of the highly heterogeneous distribution of the number of pCO₂ observations available through time (< 500 gridded cells in the 80's vs > 10 000 in the 2010's), the shape and spread of the four histograms of the residuals are closely similar between decades with a distribution centered on a global mean bias close to 0 µatm and most of the residuals falling in the -20 and 20 µatm
315   range. This demonstrates the accuracy of the method over time despite the skewed distribution of the calibration data. The analyses performed for each individual year reveal that global biases do not exceed 5 µatm. Exceptions are observed in the 80's where biases (e.g., absolute bias of 6 µatm in 1987) and RMSE (e.g., 42 µatm in 1989) can be larger and partly attributed to an exceptionally low pCO₂ observational coverage during these periods (see e.g., Bakker et al 2014). In the first version of

the coastal product (ULB-SOM-FFN-coastalv1), the evaluation of the pCO$_2$-product of Laruelle et al. (2017) was restricted to spatial and climatological seasonal cycles. In this study, we successfully extended this analysis to the entire time period and evaluated each year and decade individually.

At the regional scale, 7 out of the 10 biogeochemical provinces yield RMSEs against SOCAT_a close to 20 µatm or lower with the best fit in P2 (RMSE = 13 µatm, Table 2). This is a significant improvement over the ULB-SOM-FFN-coastalv1 product which only had 3 provinces with RMSE < 20 µatm (Laruelle et al., 2017) and none < 15 µatm. We attribute this improvement to our advanced setup of the method such as the inclusion of the atmospheric pCO$_2$ as a driver as well as an increased number of available observations to train our FFN algorithms. In three provinces (P1, P5 and P7) however, the RMSE exceeds 35 µatm. Such values can partly be explained by the complex dynamics of the sea ice in the Antarctic Shelf (P1) and by the limited number of observational data combined with the inclusion of coastal regions that present large spatiotemporal variabilities and cover two disconnected temperate basins (P5 and P7) of the Northern Hemisphere. This discrepancy was also highlighted by Landschützer et al. (2020). High discrepancies are further observed in the Baltic Sea (Figs. 2c-d) which is analyzed as a separate province (RMSE value of 43 µatm, Table 2). Excluding the Baltic Sea from P8 considerably reduces RMSE from 42 to 23 µatm. The inclusion of the Baltic Sea in P8 can likely also explain the large RMSE calculated by Laruelle et al. (2017) for the corresponding province of the ULB-SOM-FFN-coastalv1 coastal pCO$_2$-product (~ 47 µatm).

3.2 Validation against independent data

Our reconstructed coastal pCO$_2$-product is also validated against an independent dataset that is derived from pCO$_2$ observations from the SOCATv2022 that were not used for the training of the FFN algorithm (see Sect. 2.1). This dataset consists of a pool of 404,206 gridded cells that are uniformly distributed between both hemispheres (SOCAT_b, Fig. S1) and presents a good correspondence with SOCAT_a (93 % of the residuals between SOCAT_b and SOCAT_a are < 5 µatm and with a global RMSE value of 6 µatm, Fig. S2). Globally, a good match is observed between the coastal pCO$_2$-product and SOCAT_b with a global bias and a RMSE of 0 and 30 µatm, respectively. These values are similar to those derived from the statistical analysis performed against SOCAT_a. At the biogeochemical provinces scale, RMSEs generally do not exceed 23 µatm (maximum value in P6, Table 2), except where important RMSEs (~ 35 µatm for P1, P5 and P7) had already been calculated during the comparison with SOCAT_a (i.e., in regions under the sea-ice coverage dynamics and poor data coverage and provinces which encompass regions with high spatiotemporal pCO$_2$ dynamics).

As with SOCAT_a, the analysis against SOCAT_b demonstrates a good performance of our reconstructed coastal pCO$_2$-product over time with the histograms of the residuals calculated for each of the four decades presenting the same shape and spread in spite of the marked decrease of grid cells numbers over time (1054 grid cells in 80' vs 248,626 grid cell in 2010', Fig. 3b). Each of these histograms shows a distribution centered on a value of 0 µatm with 50 % of the grid cell residuals

falling between -10 and 10 µatm. This is also true at the scale of the biogeochemical provinces with the four histograms of the residuals revealing global mean biases of 0 µatm and ~ 50 % of the residual falling in the -10 and 10 µatm range. Only P8 stands as an exception (where 50 % of the residuals are between -40 and 40 µatm, Fig. S3), mainly due to the presence of the Baltic Sea in this province.

Finally, we also present pCO_2 time series derived from our reconstructed coastal pCO_2-product and compare them to data extracted from SOCAT_b for 8 coastal sites (Fig. 4). The choice of these coastal regions is motivated by their data coverage extending over 30 years (Fig. 4a) and the fact that it is possible in these grid cells to reconstruct a spatially complete seasonal climatological cycle (i.e., data are available for all 12 months). For each region, we only extracted cells for which observations extended > 30 years and reconstructed their times series from the coastal pCO_2-product and SOCAT_b, respectively (Figs. 4b-i). For most of the regions, the pCO_2-product properly captures the temporal dynamics of pCO_2 derived from the observations, bearing slight underestimations or overestimations in specific areas such as along the Cascadian shelf and the East coast of Australia (Figs. 4d and 4g). For the 8 coastal sites, absolute biases are all < 10 µatm with a minimum absolute bias of 1 µatm in the Irminger Sea and a maximum absolute bias of 9 µatm along the New Zealand coast. Except along the Cascadian Shelf, all coastal sites present RMSEs lower than ~30 µatm (5 over the 8 regions show RMSEs < ~20 µatm) which falls in the range of our global and regional RMSE values. Largest RMSE is calculated along the Cascadian shelf (62 µatm) and can partly be explained by the large spatial pCO_2 variability in SOCAT_b (as shown by the vertical bars in Fig. 4d) because of the riverine influence in the region. The overall good agreement in terms of biases and RMSEs lends confidence to our ability to unravel the long-term temporal coastal pCO_2 evolution with the newly reconstructed pCO_2-product. For example, our results show that for all the 8 studied regions, an increase in pCO_2 over time comprised between 10 and 20 µatm decade^{-1} is calculated with our pCO_2 product, a range in good agreement with the 12-18 µatm decade^{-1} obtained with SOCAT_b. Although New Zealand shows the largest bias between SOCAT_b and the pCO_2-product, they both agree that this region displays the fastest trend in terms of pCO_2 rise (18 µatm decade^{-1} and 20 µatm decade^{-1} for SOCAT_b and the pCO_2-product, respectively).

3.3 Air-sea CO_2 exchange

This section describes the coastal air-sea CO_2 exchanges patterns that are calculated using our new reconstructed pCO_2-product over the 1982-2020 period. The spatial and seasonal FCO_2 patterns are only briefly discussed (Sect. 3.3.1) since those have been extensively discussed in previous studies (see e.g., Dai et al., 2022; Resplandy et al., in rev.; Roobaert et al., 2019). We thus focus on the long-term FCO_2 trends (Sect. 3.3.2), which are still poorly understood and highly debated (e.g., Lacroix et al., 2021a; Laruelle et al., 2018; Resplandy et al., in rev.).

3.3.1 Spatial and seasonal dynamics

The spatial distribution of the climatological mean coastal FCO_2 shows that coastal regions in temperate areas (between 40°-60° in both hemisphere) and at high latitude (beyond 60° in both hemisphere) mainly act as a CO_2 sinks while CO_2 sources are

mainly encountered in the sub-tropical band (Fig. 5a) which is consistent with the global latitudinal pattern established by previous studies (e.g., Borges, 2005; Borges et al., 2005; Cai, 2011; Cao et al., 2020; Chen et al., 2013; Dai et al., 2022; Laruelle et al., 2010, 2014; Roobaert et al., 2019). Globally, with the coastal delineation used in this study ('wide coastal ocean', 76 million km²), the coastal ocean absorbs on average 0.4 Pg C per year (with an uncertainty of $\pm$ 0.03 Pg C yr^{-1}, see section 3.3.3) over the 1982-2020 period. Using the shelf break as the outer limit of the coastal domain ('narrow coastal ocean', 28 million km²) which is a more common delineation of the coastal ocean, the globally integrated coastal sink amounts to -0.2 $\pm$ 0.01 Pg C yr^{-1} which is consistent with the latest estimates (e.g., -0.2 Pg C yr^{-1} in Roobaert et al. (2019) and -0.25 Pg C yr^{-1} in Dai et al. (2022)). It should be noted that these comparisons are not straightforward because they do not cover the same time periods (i.e., 1998-2015 period in Roobaert et al. (2019), 1998-present in Dai et al. (2022) and 1982-2020 in this study) and older assessments often do not report an explicit calculation period (Regnier et al., 2022).

Most of the intense CO_2 sinks (absolute FCO_2 value > 0.5 mol C m^{-2} yr^{-1}) are encountered at high latitudes of the Northern Hemisphere and in the temperate regions of the southern Hemisphere while CO_2 sources in the tropical bands are moderate except along upwelling areas such as in the Arabian Sea (Figs. 5a and 5c). A large fraction (42 % and 50 % for the wide and narrow domain, respectively) of the global CO_2 uptake is taking place north of 60° N, which was already suggested in Laruelle et al. (2010) and further confirmed in subsequent studies (e.g., Cai, 2011; Dai et al., 2022, Laruelle et al., 2014; Roobaert et al., 2019). The spatial distribution of coastal CO_2 sources and sinks also closely follows the latitudinal FCO_2 profile calculated by Roobaert et al. (2019) which is based on ULB-SOM-FFN-coastalv1 (red and green lines in Fig. 5c). These global pCO$_2$-products however predict less variability in flux density than a compilation of regional estimations as shown in Fig. 5c when comparing our climatological FCO_2 latitudinal profile with the synthesis of 214 regional FCO_2 estimates which was already pointed by Dai et al. (2022) when comparing their data synthesis with the latitudinal FCO_2 profile of Roobaert et al. (2019) suggesting strong FCO_2 heterogeneities for a same latitudinal band. Finally, the seasonal coastal FCO_2 variability (expressed as the RMS of the seasonal amplitude,) agrees with the few studies performed at global scale (see e.g., Dai et al., 2022; Roobaert et al., 2019) with high seasonal FCO_2 amplitudes (rms values > 1.5 mol C m^{-2} yr^{-1}) at temperate and high latitudes and a low amplitude over the subtropical band (Fig. 5b).

3.3.2 Decadal trends in the coastal CO_2 sink

The rate of change in coastal FCO_2 and the various parameters involved in the FCO_2 calculation (i.e., ΔpCO_2, wind speed and sea-ice coverage) from 1982 to 2020 are presented in Fig. 6. Our results reveal significant spatial heterogeneities between the long-term temporal FCO_2 trends observed within different coastal regions, a finding consistent the range of varying slopes (including changes in sign of the slopes) already reported in local regional and discontinuous global studies (e.g., Becker et al., 2021; Laruelle et al., 2018; Wang et al., 2017). Our results also show that the decadal rates of changes in ΔpCO_2 and FCO_2 follow each other (compare Figs. 6a with 6b). Coastal regions with negative (positive) ΔpCO_2 slopes present negative (positive) FCO_2 slopes, which translate into a stronger sink/weaker source (weaker sink/stronger source). Most coastal regions (~ 70 %

of the grid cells that present a significant trend using a Mann-Kendall statistical test with a significance threshold of 95 %) exhibit negative ΔpCO_2 and FCO_2 slopes (i.e., stronger sinks or weaker sources, blue colors in Figs. 6a, b) in agreement with past studies (e.g., Laruelle et al., 2018; Resplandy et al., in rev.; Wang et al., 2017). Positives ΔpCO_2 and FCO_2 slopes (weaker

420 sink or stronger sources, red colors) can also be observed such as along the Mediterranean Sea or Southeast Asia. Stronger FCO_2 rates of change (absolute value > 0.6 mol m^{-2} yr^{-1} decade^{-1}) are mainly observed in mid-to high latitudes coastal regions and along upwelling regions (e.g., Moroccan upwelling current) while low latitudes coastal regions show weaker slopes.

Although our results suggest that the decadal change in FCO_2 intensity mainly results from that of the ΔpCO_2 (compare Fig.

425 6a with 6b), the rate of change in FCO_2 can be amplified or dampened in some regions by changes in wind speed patterns and/or sea-ice coverage (trough their effect on Eq. (1)), in agreement with recent findings by Resplandy et al. (in rev.). For most of the coastal ocean, an increase in wind speed has been observed over the study period (positive slope, red colors in Fig. 6c) with a median value for the rate of change value of 0.04 m s^{-1} decade^{-1}. This increase in wind speed promotes the FCO_2 exchange through its effect on the gas exchange transfer velocity (stronger sinks/sources). Rate changes in sea-ice coverage

430 reveal a general retreat of sea-ice in the Northern Hemisphere (negative slope, blue colors in Fig. 6d) and a gain along the Antarctic shelf (positive slope, red colors) in agreement with e.g., Serreze & Meier (2019). A decrease of sea-ice coverage favors air-sea CO_2 exchange over a larger coastal surface area and during longer periods of the year, both of which strengthen for instance the CO_2 sink in coastal regions at high latitudes of the Northern Hemisphere.

435 Globally integrated, our results indicate that today's coastal ocean has been acting as a CO_2 sink since the beginning of our study period (1982) both in the wide coastal ocean (Fig. 7a) and in the narrow domain (Fig. 7b). For both domains this CO_2 sink however increases over time. In the wide coastal ocean, the global CO_2 uptake amounted to 0.25 Pg C yr^{-1} in the 1980's (median value over the 1982-1992 period) and reached 0.52 Pg C yr^{-1} in the 2010's (mean value over the 2010-2020 period) with small interannual fluctuations (~ 0.01 Pg C yr^{-1}) of the CO_2 sink intensity diagnosed by our algorithm. The overall

440 intensification of the coastal sink that we observe in this study (0.1 Pg Cyr^{-1} decade^{-1} and 0.03 Pg C yr^{-1} decade^{-1} for the wide and narrow coastal domain, respectively) supports the only two available observational coastal studies performed at global scale (i.e., Laruelle et al., 2018; Wang et al, 2017) which were however significantly limited by the small fraction of the coastal ocean domain investigated (e.g., 6 % in Laruelle et al., 2018) and both predict an increase in efficiency of the global coastal CO_2 sink over the last three decades. Our results are also in agreement with the conceptual approach of Bauer et al. (2013) as

445 well as modeling studies, either using box models (e.g., Mackenzie et al., 2004, 2012; Rabouille et al., 2001; Ver et al., 1999) or, more recently, global ocean biogeochemical models (Bourgeois et al., 2016; Lacroix et al., 2021a, b) that all predict an increase in efficiency of the global coastal CO_2 sink at the century-scale.

The significant strengthening of this global coastal sink that we observe in this study, which has approximately doubled

450 between 1982 and 2020 (wide coastal domain) results from a general tendency towards an increase of the coastal CO_2 sinks

intensities (e.g., in the high latitude of the Northern Hemisphere, Fig. 6a) combined with decreases in intensity of several CO_2 sources such as along upwelling currents (e.g., in the Arabian sea). However, since a large fraction of the global CO_2 uptake results from coastal regions > 40° of the Northern Hemisphere and since these CO_2 sinks regions present strong negative rates of change in FCO_2 (Fig. 6a), our result suggests that the primary driver of this twofold increase of the global coastal CO_2 sink

455   is to be found in the high latitudes of the northern hemisphere, which contribute disproportionately to the global-scale coastal FCO_2 trend. However, taking the large heterogeneity in decadal FCO_2 trends, a quantitative analysis of the respective contributions of different coastal systems to the global strengthening of the coastal CO_2 sink should be performed in the future, using a regionalized approach. Moreover, changes in wind speed and sea-ice coverage have likely not been constant over time and further analysis of their influence on the rate change of FCO_2 should be analyzed for each decade individually to better

460   understand the interplay between these different drivers. Overall, our results highlight the complex nature of the coastal FCO_2 dynamics and emphasizes the need for further investigation and understanding of the specific factors influencing the FCO_2 trends in different coastal regions.

3.4 Uncertainties associated with the data-products

465   The global coastal CO_2 sink of -0.4 Pg C yr^{-1} (wide coastal domain) that we calculate in this study using the ULB-SOM-FFN-coastalv2 pCO$_2$-product is associated with a relative uncertainty that amounts to ~ 10 % (value of 0.03 Pg C yr^{-1} for σ_{FCO_2}, see Eq. (2) and Table 3). This global uncertainty mainly results from the uncertainty associated with the oceanic pCO$_2$ ($\sigma_{\Delta pCO_2}$, uncertainty of 0.02 Pg C yr^{-1}). The choice of the gas exchange transfer velocity formulation yields a 7 % difference (σ_k, uncertainty of 0.01 Pg C yr^{-1}) on the global FCO_2 calculation while we calculate a 4 % difference on FCO_2 depending on

470   the wind speed product choice (σ_{wind}, uncertainty of 0.01 Pg C yr^{-1}) or on the sea-ice product choice (σ_{ice}, uncertainty of 0.01 Pg C yr^{-1}) on the global FCO_2 calculation. Note though, that the uncertainty in the mean is substantially lower than that calculated for individual months (see Fig. 7) or regions (see e.g., discussion above regarding the Baltic Sea region) due to compensating errors as was also identified in a study by Gloege et al. (2022).

475   The total uncertainty of the oceanic pCO$_2$ (θ_{pCO_2}, value of 0.6 µatm, see Eq. (3)) mainly results from the SOM-FFN mapping method to reconstruct the coastal pCO$_2$-product (θ_{map} = 29 µatm, Table 3). This uncertainty falls within the range of values reported in the literature from different statistical interpolation methods to generate coastal pCO$_2$ data-products (RMSE values generally between 10 and 35 µatm, see Chen et al. (2016)) which are calculated from regional studies and would be expected to be smaller than those calculated for global scale analysis (or even the performance of our algorithm at the scale of its

480   provinces, which generally cover a much larger surface area than most regional studies). The θ_{map} uncertainty calculated in this study is however higher than reported for the open ocean (typical RMSE values < 20 µatm, e.g., Landschutzer et al., 2014), mainly because of the complex biogeochemical dynamics and larger variability observed in the coastal seas compared with the open ocean. We calculate a global value of 3 µatm for θ_{obs}, the uncertainty on the sampling in the field of the observations

from the SOCAT database, which is slightly higher than the value reported by Pfeil et al. (2013, value of 2 µatm). For θ_{grid},

485 the uncertainty associated with the meshing of the observations from SOCAT to gridded 0.25° monthly maps, we calculate a global mean value of 6 µatm, which is close to the value reported by Sabine et al. (2013, 5 µatm) for the open ocean. It should be noted that all these uncertainties are calculated globally and can be display large variations the regional scale (see e.g., Roobaert et al., 2019) as exemplified by the uncertainty associated with the choice of wind speed product on the FCO_2 calculation (see Roobaert et al., 2018). Moreover, due to the temporal heterogeneity of the data coverage in the SOCAT

490 database, our FCO_2 uncertainties can also vary temporally. As shown in Fig. 7, the global FCO_2 uncertainties that we report for each year (dashed black lines) are largest in the 80's (e.g., global σ_{FCO_2} value of 0.10 Pg C yr^{-1} in 1987) because of the scarcity of pCO2 measurements before 1990 in the SOCAT database and decrease over time. Our global uncertainties are also slightly larger along the nearshore domain of the coastal ocean. Using the narrow definition of the coastal domain (i.e., the shelf break as the outer limit), we calculate a global value of 0.01 Pg C yr^{-1} for σ_{FCO_2} (7 % uncertainty on the global FCO_2,

495 which is consistent with the global FCO_2 uncertainty calculated by Roobaert et al. (2019, 10 %)), 7 % FCO_2 difference depend on the k-formulation use (σ_k value of 0.01), 2 % difference on the FCO_2 calculation depending on the wind product choice (σ_{wind} = 0.002 Pg C yr^{-1}), 8 % for the sea-ice choice (σ_{ice} = 0.01 Pg C yr^{-1}), 36 µatm for θ_{map}, 8 µatm for θ_{grid} and 3 µatm for θ_{obs}.

4 Conclusions and directions for future research

500 The release of the global coastal pCO2-product in 2017 by Laruelle et al. was a significant step forward for the investigation of the spatial distribution of CO2 sources and sinks as well as their seasonal variabilities in the shallow portion of the ocean. It was also instrumental to the completion and harmonization of global ocean air-sea CO2 fluxes (Fay et al., 2021), hence supporting global carbon budget analyses (Friedlingstein et al, 2022). However, this product was not designed or evaluated regarding its ability to resolve the interannual variability and the long-term evolution of the coastal air-sea CO2 exchange,

505 which are still poorly understood (e.g., Bauer et al., 2013; Lacroix et al., 2021a; Laruelle et al., 2018; Regnier et al., 2013; Regnier et al., 2022; Resplandy et al., in rev.; Wang et al., 2017). In this study, we presented a new coastal pCO2-product for the 1982-2020 period using ~ 18 million direct coastal observations from the latest release of the SOCAT database combined with an updated version of the coastal 2-step SOM and FFN method used by Laruelle et al. (2017). We also provided a new coastal air-sea CO2 exchange product for the same period and examined the temporal evolution of the global coastal CO2 sink

510 over the past four decades. This analysis reveals that the long-term temporal trend of the air-sea pCO2 gradient drives most of the decadal evolution of the coastal CO2 sink, wind speed and sea-ice coverage playing a significant role regionally. Trends analysis of the coastal FCO_2 has also been attempted using global ocean pCO2 products that cover the coastal domain (Resplandy et al., in rev.). However, these investigation have been inconclusive, likely because global ocean pCO2-products cannot yet sufficiently well capture the specific and changing conditions occurring along the coastal domain (e.g., Chau et al,

515 2022; Rödenbeck et al., 2013 see Resplandy et al., in rev.). Our updated coastal pCO2-product circumvents these limitations

and provides a first robust assessment against which outputs from global oceanic modes results can be evaluated (e.g., Resplandy et al., in rev.). It will thus help better constrain the anthropogenic perturbation of the global ocean carbon cycle. In the future, our machine-learning approach could also be used to diagnose the main drivers of change in the global coastal ocean sink and more specifically, changes in the decadal evolution of the coastal pCO_2 field. This approach, in conjunction with

520   process-based simulations, is critically needed to evaluate and mitigate the impact of multiple anthropogenic perturbations (e.g., atmospheric pCO_2 increase, physical climate, eutrophication and hypoxia) on the global coastal carbon cycle and associated biodiversity loss and other marine stressors.

Data availability

The   ULB-SOM-FFN-coastalv2 pCO_2 and FCO_2 products   can   be   found   here:

525   https://www.ncei.noaa.gov/archive/accession/0279118 (Roobaert et al., 2023). The bathymetry derived from the 2 min global ETOPO2 database (US Department of Commerce, 2006, Table 1), the Chl-a from the monthly 4 km merged globcolour product for the 1998-2020 period from the U.U Copernicus Marine Service information (https://doi.org/10.48670/moi-00281), the SST and SSS from the daily NOAA OI SST V2 (Reynolds et al., 2007) and of the daily Hadley center EN4 SSS (Good et al., 2013), respectively. We use the dry air mixing ratio of CO_2 (xCO_2) provided by the NOAA Marine Boundary Layer

530   reference product (https://www.esrl.noaa.gov/gmd/ccgg/mbl/) assuming 100 % humidity at the air-sea interface (following calculation specified in Dickson et al., 2007) and using the NCEP reanalysis total pressure at sea level (Kalnay et al., 1996) to calculated the atmospheric pCO_2. The sea-ice coverage derived from the monthly mean of the daily 0.25° dataset of Reynolds et al. (2007), the wind speed from the 6 hours first moment of the 0.25° resolution product of the global atmospheric reanalysis ERA-interim wind product (Dee et al., 2011). The pCO_2 observations derived from the SOCAT database v2022 (Bakker et al.,

535   2022).

Author contribution

AR and GGL designed the study. AR prepared the manuscript with contributions from all co-authors.

Competing interests

The authors declare that they have no conflict of interest.

540   **Acknowledgements**

PL acknowledges support from the European Community's Horizon 2020 Project under grant agreement no. 821003 (4C). GGL is research associate of the F.R.S-FNRS at the Université Libre de Bruxelles. PR acknowledges funding from the European Union's Horizon 2020 research and innovation program under Grant agreement no. 101003536 (ESM2025— Earth System Models for the Future) and BELSPO (project ReCAP funded under the FEd-tWIN programme).

545

References

Atlas, R., Hoffman, R. N., Ardizzone, J., Leidner, S. M., Jusem, J. C., Smith, D. K., & Gombos, D. (2011). A cross-calibrated, multiplatform ocean surface wind velocity product for meteorological and oceanographic applications. *Bulletin of the American Meteorological Society*, *92*(2), 157–174. https://doi.org/10.1175/2010BAMS2946.1

Bai, Y., Cai, W. J., He, X., Zhai, W., Pan, D., Dai, M., & Yu, P. (2015). A mechanistic semi-analytical method for remotely sensing sea surface pCO2 in river-dominated coastal oceans: A case study from the East China Sea. *Journal of Geophysical Research: Oceans*, *120*(3), 2331–2349. https://doi.org/10.1002/2014JC010632

Bakker, D. C. E., Pfeil, B., Smith, K., Hankin, S., Olsen, A., Alin, S. R., Cosca, C., Harasawa, S., Kozyr, A., Nojiri, Y., O'Brien, K. M., Schuster, U., Telszewski, M., Tilbrook, B., Wada, C., Akl, J., Barbero, L., Bates, N. R., Boutin, J., … Watson, A. J. (2014). An update to the surface ocean CO2 atlas (SOCAT version 2). *Earth System Science Data*, *6*(1), 69–90. https://doi.org/10.5194/essd-6-69-2014

Bakker, D. C., Alin, S. R., Becker, M., Bittig, H. C., Castaño-Primo, R., Feely, R. A., ... & Wilson, D. (2022). Surface Ocean CO2 Atlas Database Version 2022 (SOCATv2022) (NCEI Accession 0253659).

Bauer, J. E., Cai, W., Raymond, P. A., Bianchi, T. S., Hopkinson, C. S., & Regnier, P. (2013). The changing carbon cycle of the coastal ocean. *Nature*, *504*(7478), 61. https://doi.org/10.1038/nature12857

Becker, M., Olsen, A., Landschützer, P., Omar, A., Rehder, G., Rödenbeck, C., & Skjelvan, I. (2021). The northern European shelf as an increasing net sink for CO2. *Biogeosciences*, *18*(3), 1127–1147. https://doi.org/10.5194/bg-18-1127-2021

Borges, A. V. (2005). Do we have enough pieces of the jigsaw to integrate CO_2 fluxes in the coastal ocean? *Estuaries*, *28*(1), 3–27. https://doi.org/10.1007/BF02732750

Borges, A. V., Delille, B., & Frankignoulle, M. (2005). Budgeting sinks and sources of CO_2 in the coastal ocean: Diversity of ecosystem counts. *Geophysical Research Letters*, *32*(14), 1–4. https://doi.org/10.1029/2005GL023053

Bourgeois, T., Orr, J. C., Resplandy, L., Terhaar, J., Ethé, C., Gehlen, M., & Bopp, L. (2016). Coastal-ocean uptake of anthropogenic carbon. *Biogeosciences*, *13*(14), 4167–4185. https://doi.org/https://doi.org/10.5194/bg-13-4167-2016

Cai, W. (2011). Estuarine and Coastal Ocean Carbon Paradox: CO2 Sinks or Sites of Terrestrial Carbon Incineration? *Annual Review of Marine Science*, *3*(1), 123–145. https://doi.org/10.1146/annurev-marine-120709-142723

Cao, Z., Yang, W., Zhao, Y., Guo, X., Yin, Z., Du, C., Zhao, H., & Dai, M. (2020). Diagnosis of CO2 dynamics and fluxes in global coastal oceans. *National Science Review*, *7*(4), 786–797. https://doi.org/10.1093/NSR/NWZ105

Chau, T. T. T., Gehlen, M., & Chevallier, F. (2022). A seamless ensemble-based reconstruction of surface ocean pCO2 and air-sea CO2 fluxes over the global coastal and open oceans. *Biogeosciences*, *19*(4), 1087–1109. https://doi.org/10.5194/bg-19-1087-2022

Chau, T. T. T., Gehlen M, Metzl N, & Chevallier F. (2023). CMEMS-LSCE: A global 0.25-degree, monthly reconstruction of

the surface ocean carbonate system, Earth System Data Dissc., DOI: 10.5194/essd-2023-146, in review.

Chen, C., Huang, T. H., Chen, Y. C., Bai, Y., He, X., & Kang, Y. (2013). Air-sea exchanges of CO2 in the world's coastal
580   seas. *Biogeosciences*, *10*(10), 6509–6544. https://doi.org/10.5194/bg-10-6509-2013

Chen, S., Hu, C., Byrne, R. H., Robbins, L. L., & Yang, B. (2016). Remote estimation of surface pCO2 on the West Florida
        Shelf. *Continental Shelf Research*, *128*(July), 10–25. https://doi.org/10.1016/j.csr.2016.09.004

Dai, M., Su, J., Zhao, Y., Hofmann, E. E., Cao, Z., Cai, W., Gan, J., Lacroix, F., Laruelle, G. G., Meng, F., Müller, J. D.,
        Regnier, P., Wang, G., & Wang, Z. (2022). Carbon Fluxes in the Coastal Ocean: Synthesis, Boundary Processes and
585   Future Trends. *Annual Review of Earth and Planetary Sciences*, *50*(1). https://doi.org/10.1146/annurev-earth-032320-
        090746

Dee, D. P., Uppala, S. M., Simmons, A. J., Berrisford, P., Poli, P., Kobayashi, S., Andrae, U., Balmaseda, M. A., Balsamo, G.,
        Bauer, P., Bechtold, P., Beljaars, A. C. M., van de Berg, L., Bidlot, J., Bormann, N., Delsol, C., Dragani, R., Fuentes,
        M., Geer, A. J., … Vitart, F. (2011). The ERA-Interim reanalysis: Configuration and performance of the data assimilation
590   system. *Quarterly Journal of the Royal Meteorological Society*, *137*(656), 553–597. https://doi.org/10.1002/qj.828

Dickson, A. G., Sabine, C. L., & Christian, J. R. (2007). Guide to best practices for ocean CO_2 measurements. *PICES Special
        Publication 3*, *3*(8), 191. https://doi.org/10.1159/000331784

Eldering, A., Wennberg, P. O., Crisp, D., Schimel, D. S., Gunson, M. R., Chatterjee, A., Liu, J., Schwandner, F. M., Sun, Y.,
        O'Dell, C. W., Frankenberg, C., Taylor, T., Fisher, B., Osterman, G. B., Wunch, D., Hakkarainen, J., Tamminen, J., &
595   Weir, B. (2017). The Orbiting Carbon Observatory-2 early science investigations of regional carbon dioxide fluxes.
        Science, *358*(6360). https://doi.org/10.1126/science.aam5745

Fay, A. R., Gregor, L., Landschützer, P., McKinley, G. A., Gruber, N., Gehlen, M., Iida, Y., Laruelle, G. G., Rödenbeck, C.,
        Roobaert, A., & Zeng, J. (2021). SeaFlux: Harmonization of air-sea CO2 fluxes from surface pCO2 data products using
        a standardized approach. In *Earth System Science Data* (Vol. 13, Issue 10, pp. 4693–4710). https://doi.org/10.5194/essd-
600   13-4693-2021

Friedlingstein, P., O'sullivan, M., Jones, M. W., Andrew, R. M., Gregor, L., Hauck, J., ... & Zheng, B. (2022). Global carbon
        budget 2022. Earth System Science Data Discussions, 2022, 1-159.

Gloege, L., Yan, M., Zheng, T., & McKinley, G. A. (2022). Improved Quantification of Ocean Carbon Uptake by Using
        Machine Learning to Merge Global Models and pCO2 Data. *Journal of Advances in Modeling Earth Systems*, *14*(2).
605   https://doi.org/10.1029/2021MS002620

Good, S. A., Martin, M. J., & Rayner, N. A. (2013). EN4: Quality controlled ocean temperature and salinity profiles and
        monthly objective analyses with uncertainty estimates. *Journal of Geophysical Research: Oceans*, *118*(12), 6704–6716.
        https://doi.org/10.1002/2013JC009067

Gregor, L., & Gruber, N. (2021). OceanSODA-ETHZ: A global gridded data set of the surface ocean carbonate system for

610   seasonal to decadal studies of ocean acidification. *Earth System Science Data*, *13*(2), 777–808. https://doi.org/10.5194/essd-13-777-2021

Hales, B., Strutton, P. G., Saraceno, M., Letelier, R., Takahashi, T., Feely, R., Sabine, C., & Chavez, F. (2012). Satellite-based prediction of pCO2 in coastal waters of the eastern North Pacific. *Progress in Oceanography*, *103*, 1–15. https://doi.org/10.1016/j.pocean.2012.03.001

615   Hauck, J., Zeising, M., Le Quéré, C., Gruber, N., Bakker, D. C. E., Bopp, L., Chau, T. T. T., Gürses, Ö., Ilyina, T., Landschützer, P., Lenton, A., Resplandy, L., Rödenbeck, C., Schwinger, J., & Séférian, R. (2020). Consistency and Challenges in the Ocean Carbon Sink Estimate for the Global Carbon Budget. *Frontiers in Marine Science*, *7*. https://doi.org/10.3389/fmars.2020.571720

Ho, D. T., Wanninkhof, R., Schlosser, P., Ullman, D. S., Hebert, D., & Sullivan, K. F. (2011). Toward a universal relationship

620   between wind speed and gas exchange: Gas transfer velocities measured with 3He/SF6 during the Southern Ocean Gas Exchange Experiment. *Journal of Geophysical Research: Oceans*, *116*(7), C00F04. https://doi.org/10.1029/2010JC006854

Iida, Y., Kojima, A., Takatani, Y., Nakano, T., Sugimoto, H., Midorikawa, T., & Ishii, M. (2015). Trends in pCO2 and sea–air CO2 flux over the global open oceans for the last two decades. *Journal of Oceanography*, *71*(6), 637–661.

625   https://doi.org/10.1007/s10872-015-0306-4

Jamet, C., Moulin, C., & Lefévre, N. (2007). Estimation of the oceanic pCO2 in the North Atlantic from VOS lines in-situ measurements: Parameters needed to generate seasonally mean maps. *Annales Geophysicae*, *25*(11), 2247–2257. https://doi.org/10.5194/angeo-25-2247-2007

Jones, S. D., Le Quéré, C., Rödenbeck, C., Manning, A. C., & Olsen, A. (2015). A statistical gap-filling method to interpolate

630   global monthly surface ocean carbon dioxide data. *Journal of Advances in Modeling Earth Systems*, *7*(4), 1554–1575. https://doi.org/10.1002/2014MS000416

Kalnay, E., Kanamitsu, M., Kistler, R., Collins, W., Deaven, D., Gandin, L., Iredell, M., Saha, S., White, G., Woollen, J., Zhu, Y., Chelliah, M., Ebisuzaki, W., Higgins, W., Janowiak, J., Mo, K. C., Ropelewski, C., Wang, J., Leetmaa, A., … Joseph, D. (1996). The NCEP/NCAR 40-year reanalysis project. *Bulletin of the American Meteorological Society*, *77*(3), 437–

635   471. https://doi.org/10.1175/1520-0477(1996)077<0437:TNYRP>2.0.CO;2

Lacroix, F., Ilyina, T., Laruelle, G. G., & Regnier, P. (2021a). Reconstructing the Preindustrial Coastal Carbon Cycle Through a Global Ocean Circulation Model: Was the Global Continental Shelf Already Both Autotrophic and a CO2 Sink? *Global Biogeochemical Cycles*, *35*(2), e2020GB006603. https://doi.org/10.1029/2020GB006603

Lacroix, F., Ilyina, T., Mathis, M., Laruelle, G. G., & Regnier, P. (2021b). Historical increases in land-derived nutrient inputs

640   may alleviate effects of a changing physical climate on the oceanic carbon cycle. *Global Change Biology*, *27*(21), 5491–5513. https://doi.org/10.1111/gcb.15822

Landschützer, P., Gruber, N., Bakker, D. C. E., Schuster, U., Nakaoka, S., Payne, M. R., Sasse, T., and Zeng, J.: A neural network-based estimate of the seasonal to inter-annual variability of the Atlantic Ocean carbon sink, Biogeosciences,

10, 7793–7815, https://doi.org/10.5194/bg-10-7793-2013, 2013.

645   Landschützer, P., Gruber, N., Bakker, D. C. E., & Schuster, U. (2014). Recent variability of the global ocean carbon sink. *Global Biogeochemical Cycles*, *28*(9), 927–949. https://doi.org/10.1002/2014GB004853

Landschützer, P., Gruber, N., Bakker, D. C. E., Stemmler, I., & Six, K. D. (2018). Strengthening seasonal marine CO2 variations due to increasing atmospheric CO2. *Nature Climate Change*, *8*, 146–150. https://doi.org/10.1038/s41558-017-0057-x

650   Landschützer, P., Laruelle, G. G., Roobaert, A., & Regnier, P. (2020). A uniform pCO2 climatology combining open and coastal oceans. *Earth System Science Data*, *12*(4), 2537–2553. https://doi.org/10.5194/essd-12-2537-2020

Laruelle, G. G., Cai, W., Hu, X., Gruber, N., Mackenzie, F. T., & Regnier, P. (2018). Continental shelves as a variable but increasing global sink for atmospheric carbon dioxide. *Nature Communications*, *9*(1), 454. https://doi.org/10.1038/s41467-017-02738-z

655   Laruelle, G. G., Dürr, H. H., Slomp, C. P., & Borges, A. V. (2010). Evaluation of sinks and sources of CO2 in the global coastal ocean using a spatially-explicit typology of estuaries and continental shelves. *Geophysical Research Letters*, *37*(15), 1–6. https://doi.org/10.1029/2010GL043691

Laruelle, G. G., Landschützer, P., Gruber, N., Tison, J. L., Delille, B., & Regnier, P. (2017). Global high-resolution monthly pCO2 climatology for the coastal ocean derived from neural network interpolation. *Biogeosciences*, *14*(19), 4545–4561.
660   https://doi.org/10.5194/bg-14-4545-2017

Laruelle, G. G., Lauerwald, R., Pfeil, B., & Regnier, P. (2014). Regionalized global budget of the CO2 exchange at the air-water interface in continental shelf seas. *Global Biogeochemical Cycles*, *28*, 1199–1214. https://doi.org/10.1002/2014GB004832

Laruelle, G. G., Dürr, H. H., Lauerwald, R., Hartmann, J., Slomp, C. P., Goossens, N., and Regnier, P. A. G.: Global multi-
665   scale segmentation of continental and coastal waters from the watersheds to the continental margins, Hydrol. Earth Syst. Sci., 17, 2029–2051, https://doi.org/10.5194/hess-17-2029-2013, 2013.

Mackenzie, F. T., De Carlo, E. H., & Lerman, A. (2012). Coupled C, N, P, and O Biogeochemical Cycling at the Land-Ocean Interface. In *Treatise on Estuarine and Coastal Science* (Vol. 5, Issue March 2019). https://doi.org/10.1016/B978-0-12-374711-2.00512-X

670   Mackenzie, F. T., Lerman, A., & Andersson, A. J. (2004). Past and present of sediment and carbon biogeochemical cycling models. *Biogeosciences*, *1*(1), 11–32. https://doi.org/10.5194/bg-1-11-2004

Majkut, J. D., Carter, B. R., Frölicher, T. L., Dufour, C. O., Rodgers, K. B., & Sarmiento, J. L. (2014). An observing system simulation for Southern Ocean carbon dioxide uptake. *Philosophical Transactions of the Royal Society A: Mathematical, Physical and Engineering Sciences*, *372*(2019), 20130046. https://doi.org/10.1098/rsta.2013.0046

675   Nakaoka, S., Telszewski, M., Nojiri, Y., Yasunaka, S., Miyazaki, C., Mukai, H., & Usui, N. (2013). Estimating temporal and spatial variation of ocean surface pCO2 in the North Pacific using a self-organizing map neural network technique. *Biogeosciences*, *10*(9), 6093–6106. https://doi.org/10.5194/bg-10-6093-2013

Ono, T., Saino, T., Kurita, N., & Sasaki, K. (2004). Basin-scale extrapolation of shipboard pCO2 data by using satellite SST and Chla. *International Journal of Remote Sensing*, *25*(19), 3803–3815. https://doi.org/10.1080/01431160310001657515

Park, G. H., Wanninkhof, R., Doney, S. C., Takahashi, T., Lee, K., Feely, R. A., Sabine, C. L., Triñlanes, J., & Lima, I. D. (2010). Variability of global net sea-air CO2 fluxes over the last three decades using empirical relationships. *Tellus, Series B: Chemical and Physical Meteorology*, *62*(5), 352–368. https://doi.org/10.1111/j.1600-0889.2010.00498.x

Pfeil, B., Olsen, A., Baker, D. F., Hankin, S., Koyuk, H., Kozyr, A., Malczyk, J., Manke, A., Metzl, N., Sabine, C., Akl, J., Alin, S. R., Bates, N., Bellerby, R. G. J., Borges, A., Boutin, J., Brown, P. J., Cai, W., Chavez, F. P., … Yoshikawa-Inoue, H. (2013). A uniform, quality controlled Surface Ocean CO_2 Atlas (SOCAT). *Earth System Science Data*, *5*(1), 125–143. https://doi.org/10.5194/essd-5-125-2013

Rabouille, C., Mackenzie, F. T., & Ver, L. M. (2001). Influence of the human perturbation on carbon, nitrogen, and oxygen biogeochemical cycles in the global coastal ocean. *Geochimica et Cosmochimica Acta*, *65*(21), 3615–3641. https://doi.org/10.1016/S0016-7037(01)00760-8

Rayner, N. A., Parker, D. E., Horton, E. B., Folland, C. K., Alexander, L. V., Rowell, D. P., Kent, E. C., & Kaplan, A. (2003). Global analyses of sea surface temperature, sea ice, and night marine air temperature since the late nineteenth century. *Journal of Geophysical Research*, *108*(D14), 4407. https://doi.org/10.1029/2002JD002670

Regnier, P., Friedlingstein, P., Ciais, P., Mackenzie, F. T., Gruber, N., Janssens, I. A., Laruelle, G. G., Lauerwald, R., Luyssaert, S., Andersson, A. J., Arndt, S., Arnosti, C., Borges, A. V, Dale, A. W., Gallego-Sala, A., Goddéris, Y., Goossens, N., Hartmann, J., Heinze, C., … Thullner, M. (2013). Anthropogenic perturbation of the carbon fluxes from land to ocean. *Nature Geoscience*, *6*(8), 597–607. https://doi.org/10.1038/ngeo1830

Regnier, P., Resplandy, L., Najjar, R. G., & Ciais, P. (2022). The land-to-ocean loops of the global carbon cycle. In *Nature* (Vol. 603, Issue 7901, pp. 401–410). https://doi.org/10.1038/s41586-021-04339-9

Resplandy, L., Hogikyan, A, Bange, H et al (in rev.). A Synthesis of Global Coastal Ocean Greenhouse Gas Fluxes. ESS Open Archive. April 18, 2023. DOI: 10.22541/essoar.168182303.39621839/v1

Reynolds, R. W., Smith, T. M., Liu, C., Chelton, D. B., Casey, K. S., & Schlax, M. G. (2007). Daily high-resolution-blended analyses for sea surface temperature. *Journal of Climate*, *20*(22), 5473–5496. https://doi.org/10.1175/2007JCLI1824.1

Rödenbeck, C., Bakker, D. C. E., Gruber, N., Iida, Y., Jacobson, A. R. R., Jones, S., Landschützer, P., Metzl, N., Nakaoka, S., Olsen, A., Park, G. H. H., Peylin, P., Rodgers, K. B., Sasse, T. P. P., Schuster, U., Shutler, J. D. D., Valsala, V., Wanninkhof, R., Zeng, J., & Baker, D. F. (2015). Data-based estimates of the ocean carbon sink variability - First results of the Surface Ocean pCO2 Mapping intercomparison (SOCOM). *Biogeosciences*, *12*(23), 7251–7278. https://doi.org/10.5194/bg-12-7251-2015

Rödenbeck, C., Bakker, D. C. E., Metzl, N., Olsen, A., Sabine, C., Cassar, N., Reum, F., Keeling, R. F., & Heimann, M. (2014). Interannual sea–air CO2 flux variability from an observation-driven ocean mixed-layer scheme. *Biogeosciences*, *11*(17), 4599–4613. https://doi.org/10.5194/bg-11-4599-2014

Rödenbeck, C., Keeling, R. F., Baker, D. F., Metzl, N., Olsen, A., Sabine, C., & Heimann, M. (2013). Global surface-ocean pCO2 and sea–air CO2 flux variability from an observation-driven ocean mixed-layer scheme. *Ocean Science*, *9*, 193–216. https://doi.org/10.5194/os-9-193-2013

715   Roobaert, A., Laruelle, G. G., Landschützer, P., Gruber, N., Chou, L., & Regnier, P. (2019). The Spatiotemporal Dynamics of the Sources and Sinks of CO2 in the Global Coastal Ocean. *Global Biogeochemical Cycles*, *33*, 1693–1714. https://doi.org/10.1029/2019GB006239

Roobaert, A., Laruelle, G. G., Landschützer, P., & Regnier, P. (2018). Uncertainty in the global oceanic CO_2 uptake induced by wind forcing: Quantification and spatial analysis. *Biogeosciences*, *15*(6), 1701–1720. https://doi.org/10.5194/bg-15-
720   1701-2018

Roobaert, A.; Regnier, P.; Landschützer, P., & Laruelle, G. G. (2023). A novel sea surface partial pressure of carbon dioxide (pCO₂) data product for the global coastal ocean resolving trends over the 1982-2020 period (NCEI Accession 0279118). NOAA National Centers for Environmental Information. Unpublished Dataset. https://www.ncei.noaa.gov/archive/accession/0279118. Accessed [19/06/2023].

725   Sabine, C. L., Hankin, S., Koyuk, H., Baker, D. F., Pfeil, B., Olsen, A., Metzl, N., Kozyr, A., Fassbender, A., Manke, A., Malczyk, J., Akl, J., Alin, S. R., Bellerby, R. G. J., Borges, A., Boutin, J., Brown, P. J., Cai, W., Chavez, F. P., … Yoshikawa-Inoue, H. (2013). Surface Ocean CO₂ Atlas (SOCAT) gridded data products. *Earth System Science Data*, *5*(1), 145–153. https://doi.org/10.5194/essd-5-145-2013

Sarma, V. V. S. S., Saino, T., Sasaoka, K., Nojiri, Y., Ono, T., Ishii, M., Inoue, H. Y., & Matsumoto, K. (2006). Basin-scale
730   pCO2 distribution using satellite sea surface temperature, Chl a, and climatological salinity in the North Pacific in spring and summer. *Global Biogeochemical Cycles*, *20*(3). https://doi.org/10.1029/2005GB002594

Schuster, U., McKinley, G. A., Bates, N., Chevallier, F., Doney, S. C., Fay, A. R., González-Dávila, M., Gruber, N., Jones, S., Krijnen, J., Landschützer, P., Lefèvre, N., Manizza, M., Mathis, J., Metzl, N., Olsen, A., Rios, A. F., Rödenbeck, C., Santana-Casiano, J. M., … Watson, A. J. (2013). An assessment of the Atlantic and Arctic sea–air CO2 fluxes, 1990–
735   2009. *Biogeosciences*, *10*(1), 607–627. https://doi.org/10.5194/bg-10-607-2013

Serreze MC, Meier WN. The Arctic's sea ice cover: trends, variability, predictability, and comparisons to the Antarctic. Ann N Y Acad Sci. 2019 Jan;1436(1):36-53. doi: 10.1111/nyas.13856. Epub 2018 May 28. PMID: 29806697.

Sharp, J. D., Fassbender, A. J., Carter, B. R., Lavin, P. D., & Sutton, A. J. (2022). A monthly surface pCO₂ product for the California Current Large Marine Ecosystem. *Earth System Science Data*, *14*(4), 2081–2108.
740   https://doi.org/10.5194/essd-14-2081-2022

Shutler, J. D., Land, P. E., Piolle, J. F., Woolf, D. K., Goddijn-Murphy, L., Paul, F., Girard-Ardhuin, F., Chapron, B., & Donlon, C. J. (2016). FluxEngine: A flexible processing system for calculating atmosphere-ocean carbon dioxide gas fluxes and climatologies. *Journal of Atmospheric and Oceanic Technology*, *33*(4), 741–756. https://doi.org/10.1175/JTECH-D-14-00204.1

745   Sweeney, C., Gloor, E., Jacobson, A. R., Key, R. M., McKinley, G. A., Sarmiento, J. L., & Wanninkhof, R. (2007).

Constraining global air-sea gas exchange for CO_2 with recent bomb ^{14}C measurements. *Global Biogeochemical Cycles*, *21*(2), 1–10. https://doi.org/10.1029/2006GB002784

Takahashi, T., Sutherland, S. C., & Kozyr, A. (2012). Global ocean surface water partial pressure of CO2 database: Measurements performed during 1957–2011 (Version 2011). *Carbon Dioxide Information Analysis Center, Oak Ridge National Laboratory, US Department of Energy, Oak Ridge, Tennessee,*.

Takahashi, T., Sutherland, S. C. S. C., Wanninkhof, R., Sweeney, C., Feely, R. A. R. A., Chipman, D. W. D. W., Hales, B., Friederich, G., Chavez, F., Sabine, C., Watson, A., Baker, D. F., Schuster, U., Metzl, N., Yoshikawa-Inoue, H., Ishii, M., Midorikawa, T., Nojiri, Y., Körtzinger, A., … de Baar, H. J. W. (2009). Climatological mean and decadal change in surface ocean pCO_2, and net sea-air CO_2 flux over the global oceans. *Deep Sea Research Part II: Topical Studies in Oceanography*, *56*(8), 554–577. https://doi.org/10.1016/j.dsr2.2008.12.009.Figure

US Department of Commerce, National Oceanic and Atmospheric Administration, National Geophysical Data Center, 2-minute Gridded Global Relief Data (ETOPO2v2), http://www.ngdc.noaa.gov/mgg/fliers/06mgg01.html (last access: 26 December 2022), 2006.

Ver, L. M. B., Mackenzie, F. T., & Lerman, A. (1999). Carbon cycle in the coastal zone: Effects of global perturbations and change in the past three centuries. *Chemical Geology*, *159*(1–4), 283–304. https://doi.org/10.1016/S0009-2541(99)00042-X

Wang, H., Hu, X., Cai, W. J., & Sterba-Boatwright, B. (2017). Decadal fCO2 trends in global ocean margins and adjacent boundary current-influenced areas. *Geophysical Research Letters*, *44*(17), 8962–8970. https://doi.org/10.1002/2017GL074724

Wanninkhof, R. (2014). Relationship between wind speed and gas exchange over the ocean revisited. *Limnology and Oceanography: Methods*, *12*(C5), 351–362. https://doi.org/10.1029/92JC00188

Weiss, R. F. (1974). Carbon dioxide in water and seawater: the solubility of a non-ideal gas. *Marine Chemistry*, *2*(3), 203–215. https://doi.org/10.1016/0304-4203(74)90015-2

Wrobel-Niedzwiecka, I., Kitowska, M., Makuch, P., & Markuszewski, P. (2022). The Distribution of pCO2W and Air-Sea CO2 Fluxes Using FFNN at the Continental Shelf Areas of the Arctic Ocean. Remote Sensing, 14(2). https://doi.org/10.3390/rs14020312

Zeng, J., Nojiri, Y., Landschützer, P., Telszewski, M., & Nakaoka, S. (2014). A global surface ocean fCO2 climatology based on a feed-forward neural network. *Journal of Atmospheric and Oceanic Technology*, *31*(8), 1838–1849. https://doi.org/10.1175/JTECH-D-13-00137.1

775
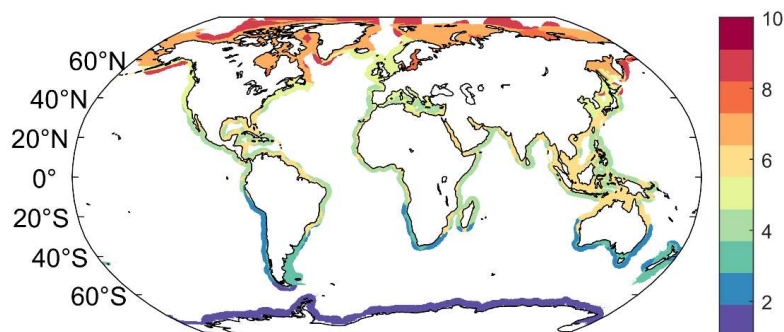
Figure 1: Coastal biogeochemical provinces generated by the Self Organizing Map clustering algorithm (SOM). The spatial extension of these provinces can vary from one month to another due to seasonal variations of the environmental drivers used during SOM. Here we present their modal spatial distribution (see Sect. 2.1 for further details).

780

Table 1: Environmental drivers used for the Self Organizing Map (SOM) and the Feed Forward Network (FFN) artificial neural networks to reconstruct the coastal pCO₂. These datasets are also used to calculate the coastal air-sea CO₂ exchange.

environmental drivers	period	resolution	manipulation	name and/or references
Sea Surface Temperature (SST, in °C)	1982-2020	0.25°, daily	monthly mean	NOAA OI SSTv2 (Reynold et al., 2007)
Sea Surface Salinity (SSS, in PSU)	1982-2020	0.25°, daily	monthly mean	EN4.2 SSS (Good et al., 2013)
Wind speed at 10 meters above sea level (U_{10}, in m s^{-1})	1982-2020	0.25°, 6 hours	monthly first moment	ERA-Interim (Dee et al., 2011)
Sea-ice coverage (ice, no unit)	1982-2020	0.25°, daily	monthly mean rate changed in sea-ice coverage	Reynolds et al. (2007)
Atmospheric pCO₂ (in μatm)	1982-2020	0.25°, monthly		NOAA Marine Boundary Layer reference product (https://www.esrl.noaa.gov/gmd/ccgg/mbl/) and Kalnay et al. (1996)
Chlorophyll a (Chl-a, in mg m^{-3})	1998-2020	4km, monthly	aggregated to 0.25°, extended the period and filled cells with no data	E.U. Copernicus Marine Service Information (https://doi.org/10.48670/moi-00281)
Bathymetry (in m)	-	2 min	aggregated to 0.25°	ETOPO2 US Department of Commerce (2006)

785
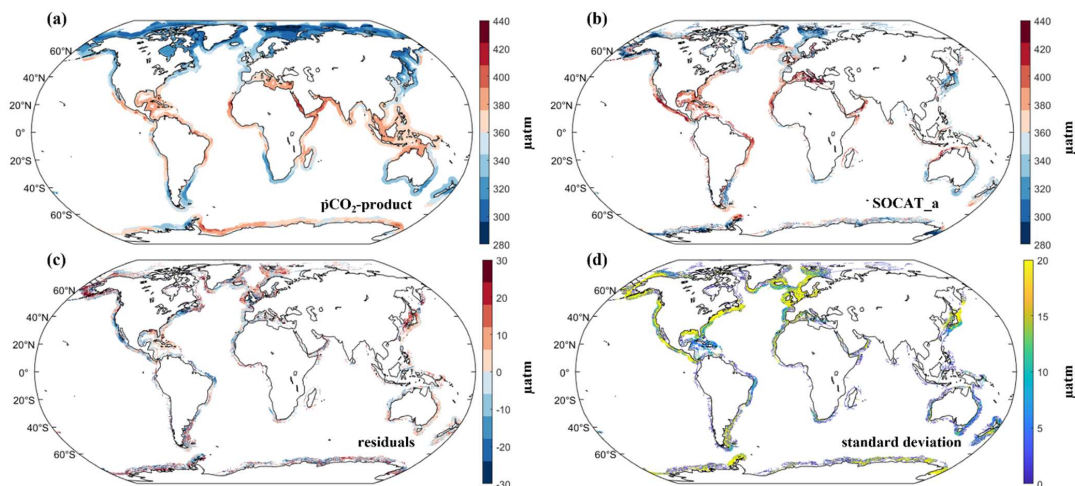
Figure 2: Global maps of the climatological (1982-2020) averaged (a) reconstructed coastal pCO₂-product, (b) gridded pCO₂ from the SOCATv2022 database and used for the FFN algorithm (SOCAT_a). (c) Temporal mean of the residuals between the coastal pCO₂-product and SOCAT_a and (d) standard deviation. All panels are expressed in µatm.
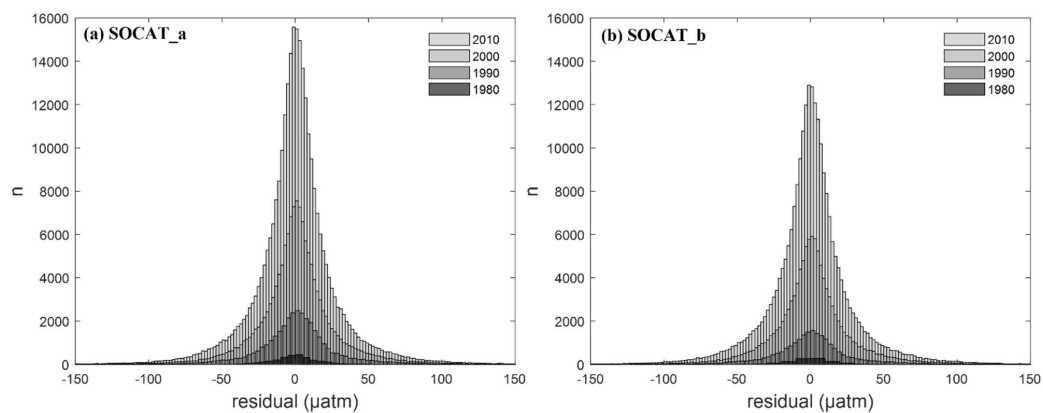
Figure 3: Histograms of the pCO₂ residuals (difference between the reconstructed coastal pCO₂-product with (a) SOCAT_a and (b) SOCAT_b) for four decades expressed in µatm.

Table 2: Statistical analyses (bias, RMSE and r²) of the reconstructed coastal pCO$_2$-product against SOCAT_a and SOCAT_b for the different biogeochemical provinces.

provinces	bias (µatm)		RMSE (µatm)		r²		cells	
	SOCAT_a	SOCAT_b	SOCAT_a	SOCAT_b	SOCAT_a	SOCAT_b	SOCAT_a	SOCAT_b
1	0.3	0.0	37	37	0.7	0.7	53256	46943
2	0.0	0.1	13	14	0.8	0.8	11868	8898
3	-0.1	0.3	21	22	0.6	0.5	35981	26032
4	-0.2	-0.3	17	17	0.8	0.8	72811	54846
5	0.1	-0.1	34	34	0.5	0.5	137754	114017
6	0.7	0.2	23	23	0.7	0.6	69032	56322
7	0.5	0.8	34	34	0.7	0.7	48704	41308
8(8*)	0.5(1.5)	0.8(1.1)	42(23)	43(24)	0.9(0.9)	0.9(0.8)	18922(1086)	18039(952)
9	-0.3	-0.2	23	22	0.8	0.8	18779	13675
10	0.1	-0.2	19	20	0.9	0.8	5009	4172
*Baltic Sea	0.5	0.7	43	43	0.9	0.9	18784	17911

*Numbers in parentheses for P8 represent statistics when the Baltic Sea is removed from P8 and defined as an isolated province.

800
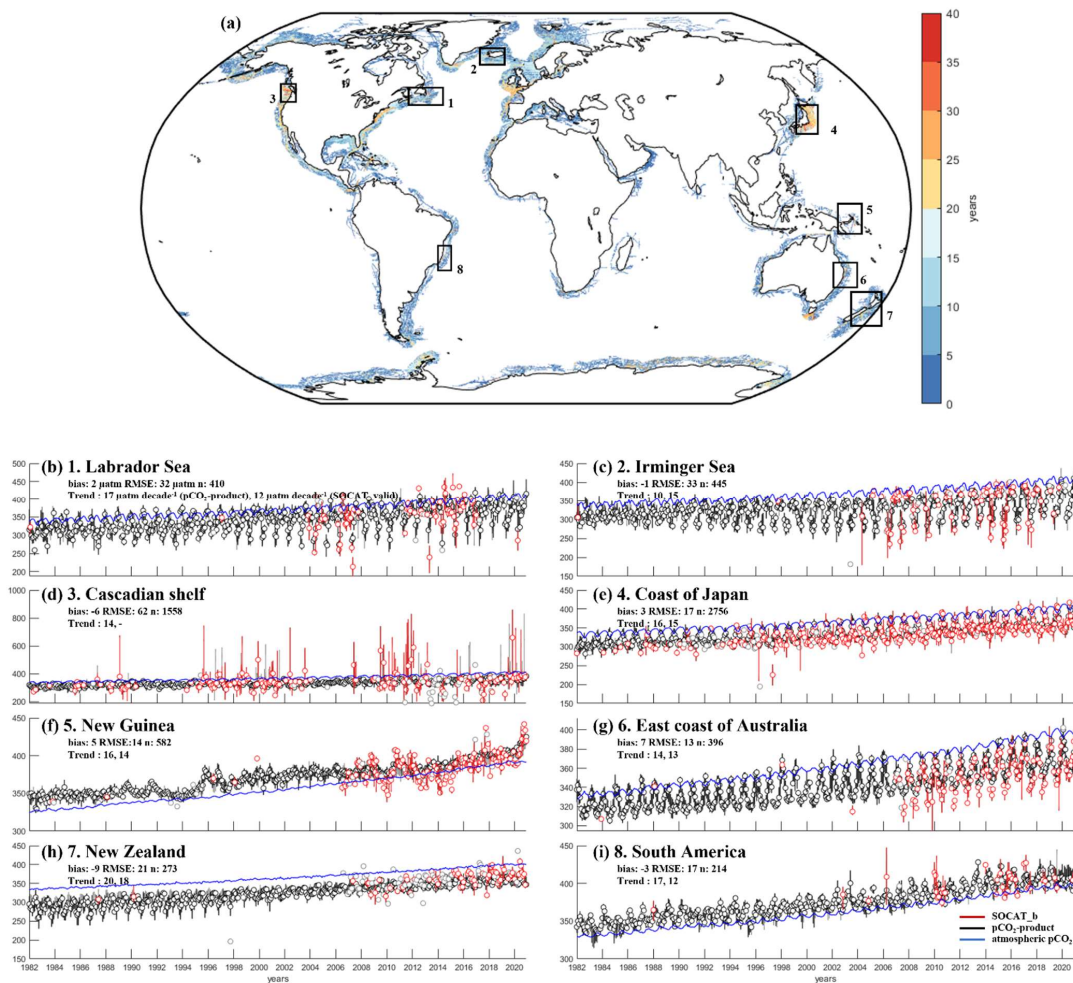
Figure 4. (a) Temporal coverage (in years) where pCO₂ measurements extend over x years in SOCAT_b. The location of the 8 coastal sites for which we present pCO₂ times series (black boxes) is also shown. (b-i) pCO₂ times series (in µatm) from the reconstructed pCO₂-product (in black), from SOCAT_b (in red), and from the atmospheric pCO₂ (in blue). For each region, we only select grid cells that extend over 30 years of observations in SOCAT_b. Medians are represented in circles and the vertical bars represent the monthly pCO₂ intra spatial variability in the region. For each region, we report the bias (µatm), RMSE (µatm) and number of cells for the calculation between the reconstructed pCO₂-product and SOCAT_b as well as their respective pCO₂ trend (in µatm decade⁻¹, which is calculate first as the slope of a linear trend using the monthly median values of the deseasonalized data). The Cascadian shelf has no value for the SOCAT_b trend since no significant trend is detected based on a Mann-Kendall statistical test.
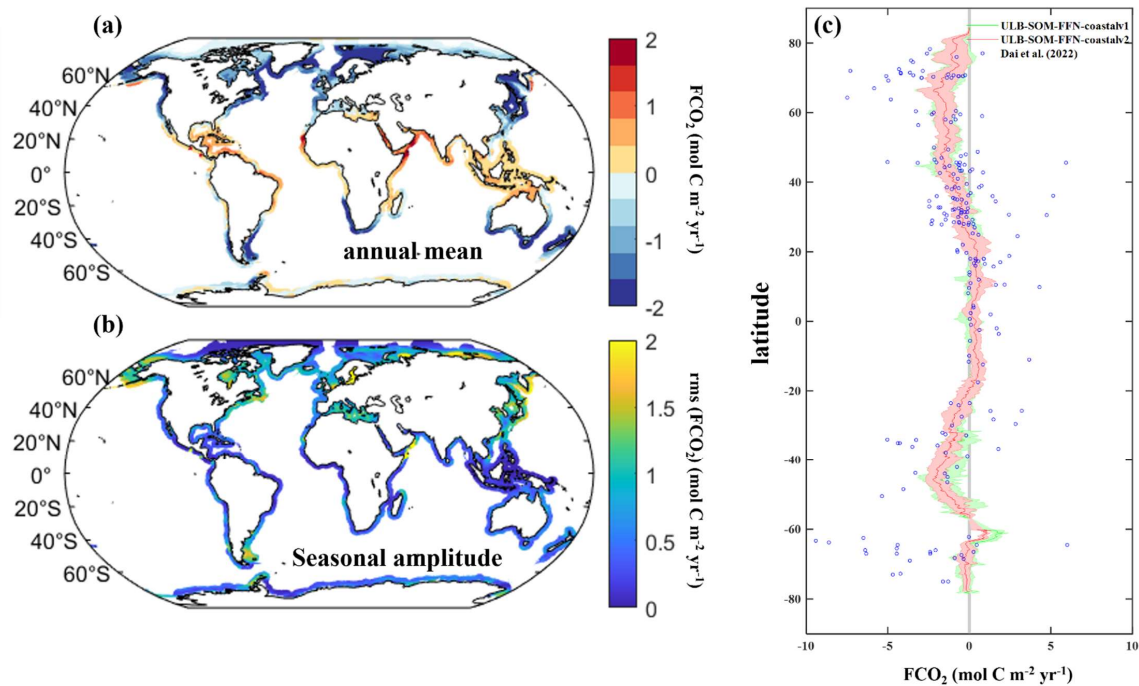
Figure 5. (a) Spatial distribution of the annual average air-sea CO₂ exchange (FCO₂, in mol C m⁻² yr⁻¹) and (b) seasonal FCO₂ variability (expressed as the Root Mean Square (RMS, mol C m⁻² yr⁻¹)) calculated with the reconstructed coastal pCO₂-product (ULB-SOM-FFN-coastalv2, 1982-2020 climatology). The latitudinal mean FCO₂ distribution (red line) and its associated longitudinal variability (red shade) is presented in panel (c). This latter is compared to the FCO₂ calculated with the ULB-SOM-FFN-coastalv1 pCO₂-product (in green, Roobaert et al., 2019) and against a synthesis of 214 regional FCO₂ estimations (Dai et al., 2022; blue dots). For consistency in the comparison in panel (c) we applied the same coastal delimitation than in Dai et al. (2022) and Roobaert et al. (2019) to the FCO₂ ULB-SOM-FFNv2 product i.e., we used the shelf break as the outer limit of the coastal domain (narrow coastal ocean). Panel (c) is also reconstructed based on an overlap period between the three products (1998-2020; except FCO₂ ULB-SOM-FFNv1 which is limited to the 1998-2015 period).
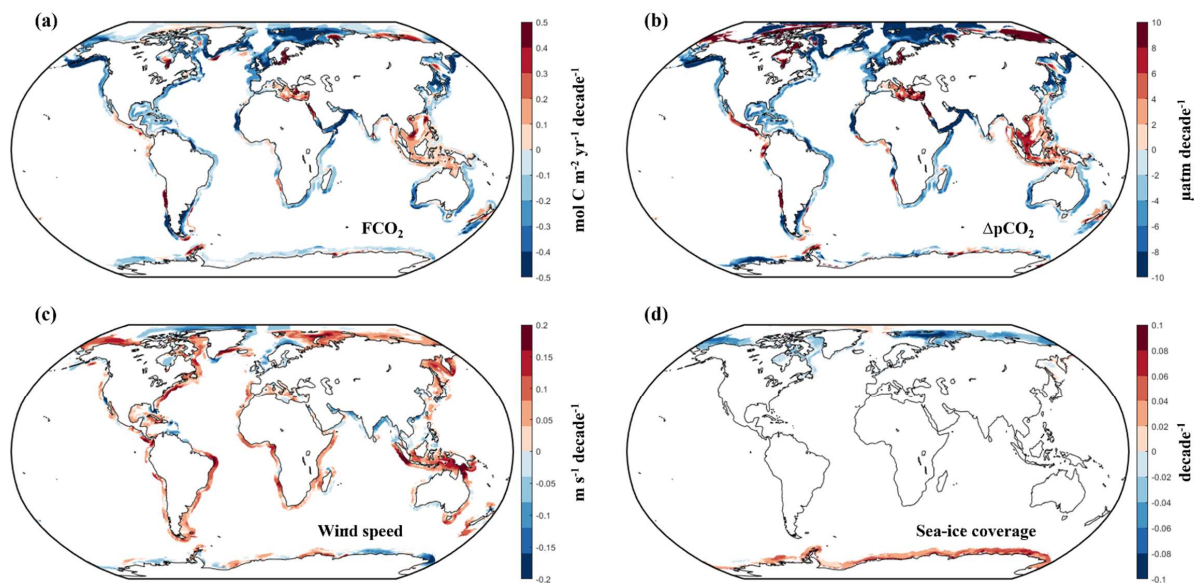
Figure 6. Rate of change in (a) coastal FCO₂ (in mol C m⁻² yr⁻¹ decade⁻¹), (b) the air-sea pCO₂ gradient (ΔpCO₂, in μatm decade⁻¹), (c) the wind speed at 10 meters above the sea surface (m s⁻¹ decade⁻¹) and (d) the sea-ice coverage (decade⁻¹) from 1982 to 2020. For each panel, the rate change is calculated as the slope of a linear regression on the monthly median values of the deseasonalized data. We only present grid cells where a significant trend is detected based on a Mann-Kendall statistical test.

830

835
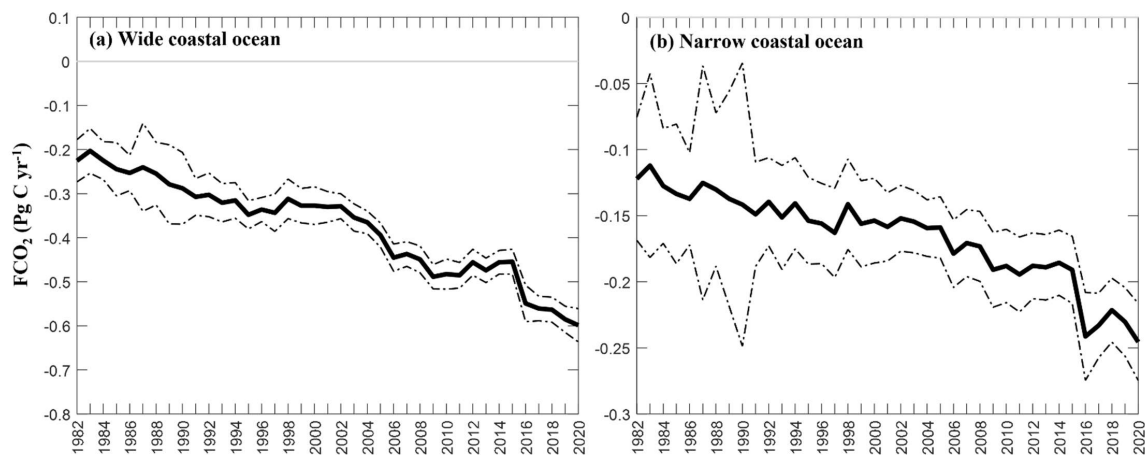
Figure 7. Evolution of the global coastal CO₂ sink (FCO₂, in Pg C yr⁻¹) over time using the reconstructed coastal pCO₂-product (black line) with its associated uncertainties (dashed black line, see Sects. 2.4 and 3.4 for further details). We use a 300 km distance from the coast as the outer limit of the coastal domain (wide coastal ocean) in panel (a) and (b) the shelf break as the outer limit of the coastal domain (narrow coastal ocean).

840

845 **Table 3. Global FCO_2 and pCO_2 uncertainties calculated for the reconstructed data-products using the wide (narrow) definition of the coastal domain.**

FCO_2 uncertainty (Pg C yr^{-1})		$\sigma_{FCO_2} = \sqrt{\sigma_{\Delta pCO_2}^2 + \sigma_k^2 + \sigma_{wind}^2 + \sigma_{ice}^2}$
σ_{FCO_2}	**0.03 (0.01)***	**Total FCO_2 uncertainty**
$\sigma_{\Delta pCO_2}$	**0.02 (0.01)**	**Uncertainty of the air-sea pCO_2 gradient**
σ_k	**0.01 (0.01)**	**Uncertainty associated with the choice of the k-formulation**
σ_{wind}	**0.01 (0.002)**	**Uncertainty associated with the choice of the wind speed product**
σ_{ice}	**0.01 (0.01)**	**Uncertainty associated with the choice of the sea-ice product**
pCO_2 uncertainty (µatm)		$\theta_{pCO_2} = \sqrt{\left(\frac{\theta_{obs}}{\sqrt{N}}\right)^2 + \left(\frac{\theta_{grid}}{\sqrt{N}}\right)^2 + \left(\frac{\theta_{map}}{\sqrt{N_{eff}}}\right)^2}$
θ_{pCO_2}	**0.6 (1.1)**	**Total uncertainty of the oceanic pCO_2**
θ_{obs}	**3 (3)**	**Uncertainty associated with the sampling on the field of the observations from the SOCAT**
θ_{grid}	**6 (8)**	**Uncertainty associated with the gridding of the observations from SOCAT into 0.25° monthly meshed maps**
θ_{map}	**29 (36)**	**Uncertainty derived from the comparison between the reconstructed pCO_2 and the observed gridded pCO_2 from the SOCAT**

* Numbers correspond to uncertainties calculated using a wide coastal delimitation, while those enclosed in brackets represent uncertainties calculated using a narrow coastal delimitation.

850